UC Santa Barbara
UC Santa Barbara Electronic Theses and Dissertations

Title

Automated Detection of Extracellular Action Potentials Propagation and Short Latency Coupling

Permalink

https://escholarship.org/uc/item/4481t747

Author

Cheng, Zhuowei

Publication Date

2022

Peer reviewed|Thesis/dissertation

eScholarship.org Powered by the California Digital Library
University of California

University of California
Santa Barbara

Automated Detection of Extracellular Action Potentials Propagation and Short Latency Coupling

A dissertation submitted in partial satisfaction
of the requirements for the degree

Doctor of Philosophy
in
Computer Science

by

Zhuowei Cheng

Committee in charge:

Professor Linda Petzold, Chair
Professor Kenneth S. Kosik
Professor Xifeng Yan

September 2022

The Dissertation of Zhuowei Cheng is approved.

Professor Kenneth S. Kosik

Professor Xifeng Yan

Professor Linda Petzold, Committee Chair

July 2022

Automated Detection of Extracellular Action Potentials Propagation and Short Latency Coupling

Copyright © 2022

by

Zhuowei Cheng

To my parents, Yunzhang Cheng and Mengjie Qiu and my grandparents, Hongkui Cheng, Zhihuan Mo, Yuhua Xiang and Chuangqiang Qiu

Acknowledgements

First off, I would like to thank my PhD advisor, Linda Petzold, not only for the years of advice and guidance, but also for her care, support and encouragement. I'm lucky to have joined the Petzold group. I would like to thank everyone in the Petzold group for their help in my research but also outside of research. We shared many good times. I also want to thank all my committee members, Linda Petzold, Kenneth Kosik and Xifeng Yan for their time and advice.

Next I would like to thank my scientific collaborators, Kosik group and Hansma group. I want to thank Kenneth Kosik for his advice and insight. He guided me in finding my topics of research. I want to thank Kenneth Tovar, Elmer Guzman, Tal Sharf, Tjitse van der Molen and Morgane Audouard for sharing their knowledge in their fields with me. I especially want to thank Kenneth Tovar for his guidance and valuable advice for my research. He helped me significantly in my work and I learned a lot from him. I want to thank Paul Hansma, not only for his advice, insight and passion in research, but also for his kindness in and outside of research. I've learned a lot through our collaboration. I want to thank Franklin Ly, Tyler Santander, Elyes Turki for the advice, discussion and the fun working together. I would also like to thank the funding agencies that funded my research.

Lastly, I want to thank my friends and family for their help and support. My parents and my grandparents have given me unconditional care and love for all my life. Without them, I would not be able to be here today. I also want to thank my husband Tie Bo Wu for his care and love everyday. I'm extremely grateful to have him by my side.

Curriculum Vitæ
Zhuowei Cheng

Education

2022	Ph.D. in Computer Science (Expected), University of California, Santa Barbara.
2020	M.S. in Computer Science, University of California, Santa Barbara.
2019	M.A. in Statistics, University of California, Santa Barbara.
2016	B.S. in Physics, Zhejiang University.

Publications

Elmer Guzman*, **Zhuowei Cheng***, Paul Hansma, Kenneth R Tovar, Linda Petzold, Kenneth S Kosik. Extracellular detection of neuronal coupling. Sci Rep. 2021 Jul

Zhuowei Cheng*, Elmer Guzman*, Paul Hansma, Kenneth S Kosik, Kenneth R Tovar, Linda Petzold. Automated detection of extracellular action potentials in single identified neurons. (Submitted)

Zhuowei Cheng, Franklin Ly, Tyler Santander, Elyes Turki, Yun Zhao, Henry Yang, Michael Miller, Paul Hansma, Linda Petzold. Preliminary Study: Quantification of Chronic Pain from Physiological Data. (Submitted)

Christopher H. Li, Franklin S. Ly, Kegan Woodhouse, John Chen, **Zhuowei Cheng**, Tyler Santander, Nirmit Ashar, Elyes Turki, Henry T. Yang, Michael Miller, Linda Petzold, and Paul K. Hansma, Dynamic Phase Extraction: Applications in Pulse Rate Variability, Applied Psychophysiology and Biofeedback (Accepted)

Xinlu Zhang, Shiyang Li, **Zhuowei Cheng**, Rachael Callcut, and Linda Petzold, Domain Adaptation for Trauma Mortality Prediction in EHRs with Feature Disparity, 2021 IEEE International Conference on Bioinformatics and Biomedicine (BIBM), 2021, pp. 1145-1152

Tal Sharf, Tjitse van der Molen, Stella M.K. Glasauer, Elmer Guzman, Alessio P. Buccino, Gabriel Luna, **Zhuowei Cheng**, Morgane Audouard, Kamalini G. Ranasinghe, Kiwamu Kudo, Srikantan S. Nagarajan, Kenneth R. Tovar, Linda R. Petzold, Andreas Hierlemann, Paul K. Hansma, Kenneth S. Kosik, Intrinsic network activity in human brain organoids. BioRXiv doi: https://doi.org/10.1101/2021.01.28.428643.

Yun Zhao, Franklin Ly, Qinghang Hong, **Zhuowei Cheng**, Tyler Santander, Henry T. Yang, Paul K. Hansma, Linda Petzold, How Much Does It Hurt: A Deep Learning Framework for Chronic Pain Score Assessment, DMBIH 2020, Sorrento, Italy, 2020.

Yun Zhao, Elmer Guzman, Morgane Audouard, **Zhuowei Cheng**, Paul K Hansma, Kenneth S. Kosik, and Linda Petzold. A Deep Learning Framework for Classification of in vitro Multi-Electrode Array Recordings. ICDM 2019, New York, USA, 2019.

W. B. Jiang, L. Yang, C. Y. Guo, Z. Hu, J. M. Lee, M. Smidman, Y. F. Wang, T. Shang, **Z. W. Cheng**, F. Gao, H. Ishii, K. D. Tsuei, Y. F. Liao, X. Lu, L. H. Tjeng, J. M. Chen, H. Q. Yuan, Crossover from a Heavy Fermion to Intermediate Valence State in Noncentrosymmetric $Yb_2Ni_{12}(P,As)_7$, Sci Rep. 2015 Dec 2;5:17608.

Abstract

Automated Detection of Extracellular Action Potentials Propagation and Short Latency Coupling

by

Zhuowei Cheng

Multi-electrode arrays (MEAs) non-invasively record extracellular action potentials (eAPs, also known as spikes) from hundreds of neurons simultaneously. We developed two algorithms that work with recordings from such devices. The first algorithm allows for automated detection of action potential propagation. Since extracellular electrodes sample from the local electrical field, each electrode can detect eAPs from multiple nearby neurons. One method to assign eAPs to their source neurons is to use spike sorting, a computational process that groups eAPs from single 'units' based on assumptions of how spike waveforms correlate with different neuronal sources, to interpret spike trains at individual electrodes of high-density arrays. However, when experimental conditions result in changes to eAP waveforms, spike sorting routines may have difficulty correlating eAPs from multiple neurons at single electrodes before and after such waveform changes. We present here a novel, empirical method for unambiguously isolating eAPs from individual, uniquely identifiable neurons, based on automated multi-point detection of action potential propagation. This method is insensitive to changes in eAP waveform morphology because it makes no assumptions about the relationship between spike waveform and neuronal source. Our algorithm for automated detection of action potential propagation produces a 'fingerprint' that uniquely identifies those spikes from each source neuron. By unambiguously isolating eAPs from multiple neurons in each recording, on a range of platforms and experimental preparations, our method now enables high-content screening with contemporary MEAs. We outline the limitations and strengths of propagation-based isolation of eAPs from single neurons and propose how our automated method complements spike sorting and could be adapted to in vivo use. Our second algorithm uses the information extracted from the first algorithm to non-invasively detect synaptic relationships among neurons from in vitro networks. Our methods identify short latency spiking relationships between neurons with properties expected of synaptically coupled neurons, namely they were recapitulated by direct stimulation and were sensitive to changing the number of active synaptic sites. Our methods enabled us to assemble a functional subset of neuronal connectivity in our cultures.

Contents

Chapter 1

Introduction

Extracellular recording of action potentials has been used for decades, and has revealed fundamental insights in cellular and sensory neuroscience [1, 2, 3]. The relative ease of use and the non-invasive nature of extracellular recording makes this technique technically approachable for recording action potentials from groups of excitable cells, compared to other electrophysiological recording configurations. Recent progress in fabrication and surface chemistry have led to the production of 2- and 3-dimensional extracellular electrode arrays, consisting of hundreds to thousands of densely-packed electrodes [4, 5]. Arrays such as these have been used to record simultaneously from hundreds of cultured primary neurons or iPS-derived neurons grown on these substrates [6, 7], as well as from intact brains [8, 9]. However, the burden of increased data handling and computational cost accompany the increase in data channels, particularly when experiments require significant post-acquisition data processing [10, 11].

Since extracellular electrodes sample from the electric field, rather than directly from each neuron, these electrodes detect eAPs from any proximal neuron. The likelihood that each electrode detects eAPs from multiple neurons increases with the density of neurons, compromising an electrode's ability to isolate eAPs from single sources. Computational approaches collectively known as spike sorting have been developed to isolate, or sort, eAPs into discrete source 'units' [12, 13]. Multiple sorting routines have been introduced to automate data processing from arrays with several thousand electrodes [11, 14, 15]. Many such sorting routines assume that characteristics of the eAP waveforms from each electrode correlate with properties from each source neuron [12, 10, 13, 16]. These assumptions are multiplied in recordings with thousands of electrodes, from neurons at high density. In different experimental preparations, ground truth validation of how sorting routines isolate spikes can only be achieved with technically challenging experiments that, for example, pair extracellular recording with intracellular or juxtacellular recording [15]. Additionally, eAP waveforms from individual neurons can vary significantly within a single recording session due to changes, for example, in firing frequency [17, 18]. Common experimental manipulations that change eAP waveforms make it challenging for sorting routines to follow the same isolated 'unit' between experimental manipulations [19, 20]. Efforts to validate the assumptions intrinsic to spike sorting routines are ongoing [21]. However, the ability of any sorting routine to reliably isolate spikes from the same neuronal source during experiments that significantly change waveform shape remains largely untested.

We previously used detection of action potential propagation among extracellular electrodes to uniquely identify, isolate and characterize propagating eAPs from individual cultured neurons [22]. Because axonal action potential propagation is unidirectional, the sequence of eAP occurrences at each array electrode along the propagation path creates a 'fingerprint' that identifies each detected neuron. Here we present the automation of this empirical approach to isolating eAPs from multiple uniquely identifiable neurons in large electrode arrays. Detection of eAP propagation among extracellular electrodes categorizes ensemble spiking data into eAPs from unique source neurons, and for the first time routinely provides ground truth for the isolation of eAPs in extracellular recordings.

Our algorithm is based on the eAP propagation path across multiple electrodes. The electrodes in each propagation cohort, the order of eAP occurrence and the eAP latency between each electrode are features that identify each signal. We also refer to the action potentials detected by these electrode cohorts as propagation signals.

Our method reliably detects the same source neuron between experimental conditions that affect spike morphology [23], including high spiking frequency, temperature changes or drugs such as K^+ channel blockers. Our method reveals multiple unique neurons in recordings from primary cultures grown on low- or high-density arrays, as well as from whole human brain organoids recorded with shank electrode arrays. Automated detection of propagation separates propagating eAPs in identified source neurons from all other spikes in any extracellular recording and enables tracking single neurons across experimental conditions. Our algorithm enhances and streamlines post-acquisition data handling because propagating eAPs from single neurons seen at multiple electrodes are redundant in terms of extracting a neuron's spiking pattern. Our algorithm can also be used in combination with traditional spike sorting routines and redundant eAPs identified by our algorithm can be ignored by spike sorting routines.

Oftentimes, multiple unique propagation signals are present on each array in our experiments. Here we also examined the intercellular relationships between single cultured mouse hippocampal neurons isolated by their distinctive propagation signals and eAPs at all other array electrodes.

Superimposing the eAPs from constituent propagation signal electrodes corresponding to each unique neuron effectively recalibrates the timing of the voltage record from all other array electrodes to the propagation signal spike times. Isolating spiking from single identified neurons in this way revealed clusters of spikes at other electrodes occurring within milliseconds of the preceding propagation signal spike. We studied the underlying nature of these associations in spike timing by using stimulation, by decreasing the probability of neurotransmitter release and by changing the recording temperature. Our results are consistent with direct synaptic coupling underlying many of the short latency relationships between propagation signal spikes and the spike clusters at other electrodes. The amplitude distributions of the coupled eAP clusters are often statistically discrete subsets of the full eAP amplitude distribution at those electrodes, consistent with coupled spikes representing eAPs from single postsynaptic neurons. Our results suggest that in our in vitro system, axons can make a sufficient number of synapses on postsynaptic neurons to result in firing of those neurons. Our methods can be generalized to reveal in vitro network connectivity phenotypes from targeted mutant or iPS-derived neurons that might be overlooked by more traditional experimental approaches.

Details of use of our algorithms, along with documentation, can be found at
https://github.com/ZhuoweiCheng/Propagation-Signal-and-Synaptic-Coupling-Algorithm

The content in this dissertation is the result of a collaboration with Kenneth Tovar and Elmer Guzman. The content in chapter 3 is the result of a collaboration with Elmer Guzman and has appeared in Scientific Reports [24]. The rest is expected to appear in publication as well.

Chapter 2

Automated detection of extracellular action potentials from single neurons

2.1 Results

2.1.1 Detection of action potential propagation identifies single neuron eAPs

In this work we used previously characterized features of action potential propagation detection on MEAs [22] to design an algorithm that automates isolation of spikes from single neurons. Action potential propagation is evident in arrays of extracellular electrodes by the repeated co-occurrence of eAPs at multiple electrodes[22, 25]. The propagation sequence among cohort electrodes identifies such eAPs as originating from each unique source neuron. Every recording from primary neurons cultured on arrays we examined had multiple unique examples of action potential propagation in multiple neurons, reflected by eAPs among electrode cohorts. Figure 2.1A shows a portion of an electrode array with black circles indicating a cohort of electrodes at which propagating action potentials from a single neuron were detected. The unidirectionality and high fidelity of action potential propagation results in the invariant sequence detection (Figure 2.1B) and low inter-electrode latency variability of these eAPs (Figure 2.1C). In this example, manual analysis showed that 93.3% (1939/2078) of the eAPs in electrode 1 were followed by eAPs in electrode 2, with a mean latency of 0.255 ± 0.018 ms. Similarly, 92.0% (1912/2078) of the eAPs at electrode 1 were followed by eAPs at electrode 3, with a mean latency of 0.485 ± 0.037 ms, and 76.2% (1583/2078) of the eAPs at electrode 1 were followed by eAPs at electrode 4, with a mean latency of 0.534 ± 0.047 ms (Figure 2.1C). Manual assessment of eAP co-occurrences was done by comparing the eAP times in electrode 1 with spike times at other cohort electrodes and excluding inter-electrode latencies greater than 1 ms. The coefficients of variation (CV) of the latencies in this example (0.071, 0.076 and 0.088 respectively) are consistent with a high fidelity process like action potential propagation.

To test whether the latencies between eAPs at electrode 1 and eAPs at the other electrodes resulted from random alignment, we shuffled the spike times of eAPs at electrodes 2, 3 and 4 while retaining the identical inter-spike interval (ISI) distribution of those electrodes (Figure 2.1D). In the shuffled data, there were only 49, 69 and 92 eAPs (for electrodes 2, 3 and 4, respectively) with latencies below 1.5 ms (0.68 ± 0.44 ms, 0.76 ± 0.45 ms and 0.77 ± 0.46 ms respectively). These results suggest that the high number of eAPs at electrodes 2, 3 and 4 with sub-millisecond latency from electrode 1 were unlikely to result from random alignment of spikes and are instead consistent with action potential propagation among these electrodes.

Our automated method uses the invariant unidirectionality of eAP detection and low inter-electrode latency to isolate each electrode cohort of propagating eAPs. The sequence of eAP propagation among these electrodes uniquely identifies each unique eAP cohort. The algorithm first constructs cross-correlograms between a reference electrode and all

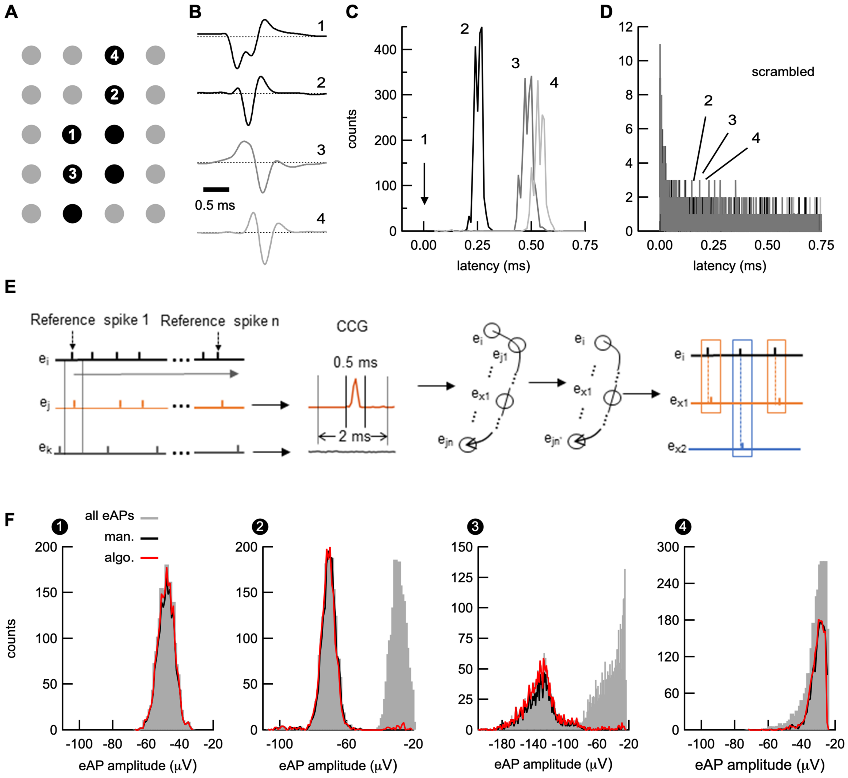

Figure 2.1: Automated detection of eAP propagation. A, Action potential propagation was manually detected among electrodes indicated by black dots. B, shows averaged eAP waveforms from the electrodes indicated in A. The time offset of the eAP peaks, from top to bottom, illustrate propagation among the indicated electrodes. Each waveform represents the average of 90-100 sweeps and averaged waveforms were scaled to the same amplitude for the sake of clarity. C, shows the eAP latency distribution between propagating eAPs at electrode 1 and electrodes 2, 3, and 4, respectively. Panel D shows the latency distribution of scrambled eAP times from C, showing very few scrambled spikes occur at this short latency. Scrambled eAP latency distributions for electrodes 1-3 are superimposed. Note the difference in y-axis between C and D. These features are used for automated detection, as outlined in E. F compares results from manual detection of action potential propagation (black lines) and the results from our algorithm (red lines) by overlaying each on the all-points eAP amplitude histograms (grey) from the electrodes in our example. Note the small fraction of potentially mis-detected eAPs for manual and automated detection outside of the main modes in the middle histograms. This recording was done on a low electrode density array (120 electrodes; 100 μm pitch) from cultured mouse hippocampal neurons. Bin sizes in C and D were 0.1 ms. Bin sizes in F were 1 μV.

other electrodes to find candidate constituent electrodes from each cohort of propagating eAPs (Figure 2.1E). In every iteration, each electrode is used as a reference electrode, to compare with all other electrodes. A collection of electrodes representing the path of eAP propagation is then generated. Within each such electrode cohort, the number of short latency (<1.5 ms) co-occurrences between eAPs at the reference electrode and eAPs at all other electrodes are compared. The maximum number of eAP co-occurrences between the reference electrode and any other cohort electrode approximates the spike times for that electrode cohort. We refer to these two electrodes as anchor points, and the electrode with the earliest eAPs in the propagation sequence as anchor point 1. A second scanning step reduces false positive electrodes by eliminating electrodes with a low fraction of co-occurrences. The algorithm outputs cohort electrodes along with statistics for each unique cohort detected, including spike times of each isolated spike train, inter-electrode latencies and number of co-occurrences between the reference electrode and other electrodes. Details of user-defined settings for detection parameters refinement, as well as criteria for selecting candidate electrodes are described in the Methodology section.

The histograms in Figure 2.1F show the amplitudes of all spikes at electrodes 1 through 4 (grey). Superimposed on these distributions is a comparison at each electrode of the results of manually detected short latency eAPs and the isolated eAPs from automated detection (black and red lines, respectively). Automated and manual analysis revealed that the majority of eAPs in electrode 1 were followed with short latency by eAPs in the other electrodes. For automated detection, 97.1% of the eAPs at electrode 1 were followed by eAPs in electrode 2, 95.9% were followed by eAPs in electrode 3 and 78.3% were followed by eAPs in electrode 4 (red lines in each histogram). Using manual detection, these values were 93.3%, 92.0% and 76.2% respectively (black lines in each histogram). This comparison demonstrates that results from automated action potential propagation detection are at least as good by virtue of amplitude and timing information, as the far more error-prone and laborious process of manual comparison of spike times from different electrodes.

Because detection of action potential propagation confirms eAPs as resulting from a single neuronal source, the narrow eAP amplitude distribution in electrode 1, coupled with the high number of co-occurrences (>97%) detected suggests that this amplitude distribution represents eAPs from a single neuron. In contrast, the eAP amplitude distribution from electrode 2 is divided into two discrete modes. Automated detection revealed that the eAPs in electrode 2 which occurred with short latency (1980/3864) from eAPs in electrode 1 were limited almost exclusively to one mode of the electrode 2 distribution (red line). If random alignment of spikes explains the short latency between eAPs in electrodes 1 and 2, the eAP amplitudes would be evenly distributed between both modes of the electrode 2 distribution. However, these short latency eAPs were limited to an apparent single mode, consistent with a single neuronal source of those eAPs. Propagating eAPs at electrode 3 that were isolated either by our algorithm or manually were limited to the same single amplitude distribution component (red and black lines) and overlapped each other almost uniformly. Unlike the eAP amplitude distributions from electrodes 2 or 3, the amplitude distribution at electrode 4 appears to be a single mode, part of which was excluded by the detection threshold for this electrode, which likely explains why fewer eAP co-occurrences between electrode 1 and 4 were found with either detection method. As with electrodes 2 and 3, amplitude distributions from automated and manually isolated eAPs almost completely overlap each other at electrode 4 (red and black lines). Interestingly, though the electrode 4 eAP amplitude distribution appears unimodal, our results indicate that spikes from at least 2 neurons were detected at this electrode, highlighting the unreliability of amplitude distribution shape as criteria to estimate the number of neurons at an electrode. These results demonstrate that automated detection of action potential propagation yields results that are, at minimum, as good as results from the much more time consuming and error-prone manual detection.

2.1.2 Detection probability and spike train refinement

Our method for isolating eAPs from individual neurons is based on detection of action potential propagation between at least 2 electrodes. The reliability of neuronal spike trains isolated by our method is therefore sensitive to the signal-to-noise characteristics of cohort electrodes. Assume, for example, that eAPs at the first electrode have an infinitely high signal-to-noise ratio and propagating eAPs at the second electrode have a mean amplitude of 1.5 times the detection threshold, with a standard deviation that is 33% the eAP amplitude. The co-detection requirement means that in this example, the number of propagating eAPs detected will be under-sampled by at least 16% below the number of eAPs at first electrode, resulting in gaps in the spike train.

We used co-detection of eAPs in the first two anchor points to determine how eAP detection probability varies with the signal-to-noise ratio at the other cohort electrodes from our algorithm. For this analysis, the set S is the co-occurring eAPs between the anchor point 1 and any other cohort electrode giving the most co-occurrences. The set S is a proxy representing the maximum number of eAPs detected from each neuron. The detection probability for all other electrodes in the same cohort is defined as the ratio of the number of co-occurrences between eAPs at that electrode and S to the number of eAPs in S.

A map of coactive electrodes for a propagating eAP is shown in Figure 2.2A (black circles). Figure 2.2B displays the average waveforms from electrodes 1, 2 and 3. Waveforms are ordered from left to right by their eAP amplitude/detection threshold ratios. As expected [26], the detection probability rises steeply with increasing value of the eAP amplitude/detection threshold ratios (Figure 2.2C). This plot includes data from 1030 electrodes of 750 unique propagating eAPs in 63 recordings from neurons on low density arrays (120 electrodes; 100 μm pitch). Red dots are values from the example eAP waveforms (Figure 2.2B). Failures of propagation cannot be ruled out as occasionally contributing to failures to detect eAPs at cohort electrodes[27, 28]. However, given the high coefficient of variation of the amplitude/threshold ratio (1.73 ± 0.91, n = 1030) and the high fidelity of action potential propagation [29, 30], the occasional absence of expected propagating eAPs at a cohort electrode (Figure 2.2C) is consistent with a failure of spike detection. The results reported here with automated eAP propagation detection recapitulate results previously obtained manually [22].

These results demonstrate that to maximally represent spike trains from isolated neurons, selecting coactive electrodes with high detection probability is crucial. The relationship between eAP detection probability and the eAP amplitude/threshold ratio may result in under-sampling spikes, thus creating gaps in the spike train. However, if detection failures at any electrode occur randomly, then detection failures at cohort electrodes would not be expected to occur simultaneously (Figure 2.2D). To minimize gaps in the spike train resulting from failures of spike detection, we examined whether adding anchor points improves the results of the automated detection of eAP propagation algorithm. The algorithm first identified constituent electrodes of eAP propagation. Co-occurrences between eAPs at the first 2 anchor points (S) are used to approximate the number and timing of propagating spikes. We used the same 1.5 ms detection limit following the eAP at anchor point 1. Cohort electrodes were ordered based on the number of co-occurrences with anchor point 1. The electrode with the most co-occurrence is designated anchor point 2. The propagating eAP spike times of anchor point 1 are the best representation of the spike train from that neuron, due to the high signal-to-noise ratio near action potential initiation [31]. We tested the effect of adding additional

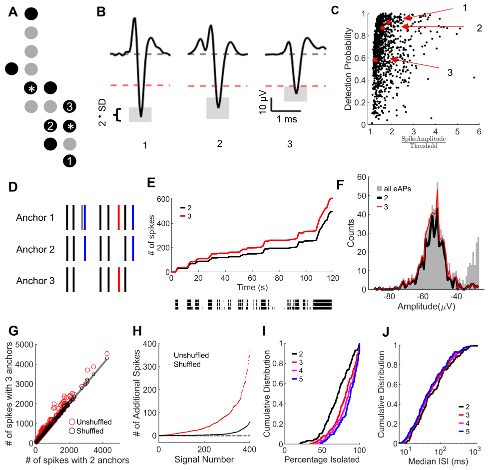

Figure 2.2: A, Map of constituent electrodes (black circles) for the subset of propagating eAPs. The two anchor points are marked with $*$. B, Average of 1000 propagating eAP waveforms from electrodes 1, 2 and 3 in (A). Time and amplitude axes are the same for each waveform. Dashed black lines are the baseline (0 μV). Red dashed lines represent the specific spike detection threshold at each electrode. The grey areas indicate ± one standard deviation of the eAP amplitude. C, the detection probability versus eAP amplitude/the eAP detection threshold ratios. Each black dot represents one constituent electrode of an eAP propagation and the red dots are results from electrode 1, 2 and 3 from B. 7 dots with a spike amplitude to threshold ratio over 6 were omitted to highlight the majority of the data. D, A raster plot of the first three anchor point electrodes from one eAP propagation. In this example, black lines indicate co-occurring spikes detected by all three electrodes, blue lines show co-occurrences detected only by the first two anchors and red lines are detected with the use of a third electrode. Grey line is an eAP at anchor 1 with no co-occurrences with anchor 2 or 3. E, shows the number of propagating eAPs detected during a recording by using 2 versus 3 anchor points. The raster plot for the three anchor points in this example is below, with anchor 1, 2 and 3 from top to bottom. F, shows the histogram of all eAP amplitudes (grey) in anchor 1 from E. The resulting propagating eAP amplitude distributions isolated using 2 (black line) or 3 (red line) anchors are superimposed. G, compares the number of propagating eAPs isolated when using three anchor electrodes versus the number of propagating eAPs isolated using two anchor electrodes (red circles). The results of shuffling the eAP times on anchor 3 are superimposed (black circles). The slope of the grey line is equal to 1. H, compares the additional propagating eAPs detected by adding a third anchor in shuffled versus unshuffled data. All dots are in ascending order by the number of eAPs added by including a third anchor. I, Percentage of propagating spikes isolated over the total number of spikes on anchor 1 for each eAP propagations using 2, 3, 4 or 5 anchors. J: The median ISI of the same eAP propagation using 2, 3, 4 or 5 anchors as in I. All data in this figure were from recordings done on low electrode density arrays from cultured mouse hippocampal neurons.

anchor points, from most to least co-occurrences with anchor 1. Co-occurrences between additional anchor points and anchor point 1 are added to S to comprise an amended set of propagating eAPs.

The schematic (Figure 2.2D) illustrates the effect of using two versus three anchor points. In this example, if propagation is defined by eAP co-occurrences at anchor 1 and anchor 2, then 7 eAPs will be isolated. Including anchor 3 increases the total to 8 eAPs. Figure 2.2E compares the effect of using 2 versus 3 electrodes to reduce artifactual gaps in the spike train. Using 3 anchor points results in more isolated eAPs (Figure 2.2E) compared to using 2 anchor points, as shown by the progressively greater increase in number of propagating eAPs during the recording. The amplitude distribution of the extracted eAPs from anchor 1 from this example (Figure 2.2F) shows that spikes isolated with the addition of a third electrode occur in the same amplitude mode, indicating that those eAPs are from the same single neuronal source. At the anchor point 2 electrode, the mean amplitude of propagating eAP was -89.7 ± 10.0 μV and the threshold was -24.1 μV which should allow us to isolate almost all propagating eAPs (Figure 2.2C). However, including propagating eAPs from anchor point 3, (-35.0 ± 4.9 μV mean amplitude; -24.8 μV threshold) still increased the total number of propagating spikes that were isolated by our algorithm, demonstrating how gaps in the spike train were filled by increasing the number of anchor points when possible.

Using more than 2 anchor points reduced the number of undetected propagating eAPs but could also introduce artifactually detected eAPs to the spike train. To test the extent to which such co-occurrences added by a third anchor point represent random eAP alignment between anchor point electrodes, we shuffled the timing data at the third electrode, then determined the number of eAPs added to the propagation spike train (Figure 2.2G). Data shuffling was done by retaining the ISI distribution but shuffling the spike time. This was done with 414 eAP propagations that had at least three constituent electrodes, from the same 63 recordings. If inclusion of a third anchor point produces no increase in the spike total, then all points will lie on the line with the slope equal to 1 (grey line). The number of spikes added when including a third anchor point increased more in the unshuffled spike set (red dots) than in the shuffled spike set (grey dots). A direct comparison of the number of additional spikes with or without shuffling (Figure 2.2H) indicates that shuffling only occasionally increased the number of spikes, whereas using a third anchor point almost always added eAPs to each spike train (Figure 2.2H). For example, in 138/414 neurons, using 3 anchor points increased the number of propagating eAPs by at least 20% compared to using 2 anchor points. In contrast, shuffling the spike times at the third electrode resulted in a 20% or greater increase in additional eAPs in only 4/414 neurons. In unshuffled data, using 3 anchor points resulted in a 30% or greater addition of propagating eAPs in 86/414 neurons whereas there was never any increase in the number of spikes greater than 30% in the shuffled data. These results demonstrate that random alignment of eAPs is not a significant source of spikes added when using a third anchor point.

Increasing the number of anchor points produce significant refinements in spike rate detection of the propagating eAPs in our data. We therefore examined the result of adding additional electrodes in the same data set by comparing the results of using 2, 3, 4 or 5 anchor points. Increasing the number of anchor points results in a gradual increase in the percentage of propagating eAPs isolated (Figure 2.2I). In this data set (144 eAP propagations with at least 5 cohort electrodes) the increase from 2 and 3 anchor points diminishes when adding 4 or 5 anchor points. The median ISIs from the same 144 eAP propagations comparing the number of anchor points results in relatively minor differences above 3 anchor points (Figure 2.2J). For different use cases, the number of anchor points in our algorithm is a user-defined variable. Our results demonstrate that most propagating eAPs can be found with just two anchor points. However, using more anchor points refines the extracted spike train, resulting in fewer gaps due to detection failures, with diminishing differences above 3 anchor points in this data set.

2.1.3 Automated detection of propagating eAPs is insensitive to frequency-dependent changes in eAP waveform

Transmembrane action potentials in many types of neurons show frequency-dependent changes in amplitude or spike width [32, 33]. Frequency-dependent changes are reflected in the extracellularly recorded action potentials from these neurons [17, 34]. Spike sorting routines could interpret frequency-dependent eAP waveform heterogeneity from single neurons as action potentials from multiple neuronal sources. The problem for spike sorting resulting from heterogeneity in action potential waveform in single neurons has been discussed elsewhere [19, 18]. Unlike spike sorting routines, detection of action potential propagation reliably isolates spikes from single neurons when frequency-dependent changes in eAP waveform occur (Figure 2.3). This example illustrates that a burst of propagating action potentials in one constituent electrode (Figure 2.3A) results in a frequency-dependent decrease in spike amplitude (Figure 2.3B) and an increase in spike width (Figure 2.3C). Note the change in the peak-to-peak latency of eAPs that occurred following ISIs $\geq$ 500 ms, compared to the latency for eAPs following ISIs of $\leq$ 30 ms (brackets, Figure 2.3C). This difference likely reflects decreased Na^+ channel availability at high spike frequency[35]. As shown, our method of detecting action potential propagation isolates eAPs from single neurons at inter-spike intervals as short as 2 ms (Figure 2.3D), just above the refractory period frequency cutoff we used for spike detection. The cumulative distribution of inter-spike intervals (ISI) shows that in this recording, 64% of all the spikes (open grey circles) occurred following ISIs from 30 to 500 ms. The plot of eAP amplitude as a function of ISI shows the amplitude variability in this intermediate frequency domain (Figure 2.3E). For example, for the propagating spikes in the anchor point 1 electrode (closed circles) that follows intervals between 30 to 500 ms had a mean amplitude of -54.9 ± 15.8 μV (n = 552). At the anchor point 2 electrode (open circles) in the propagation pathway from this example, the mean amplitude of propagating spikes (from anchor point 1) occurring within intervals of 30 to 500 ms was -61.7426 ± 21.5336 μV (n = 554), mirroring the amplitude variability in eAPs in the anchor point 1 electrode. Because eAP morphology is expected to vary with inter-spike interval [17], the variability of spike shapes in this large frequency range may present as eAPs from multiple units for spike sorting. However, our algorithm detected action potential propagation in this neuron across more than three orders of magnitude of inter-spike intervals (Figure 2.3D, E).

2.1.4 Automated detection of propagating eAPs is insensitive to experimentally-induced changes in waveform shape

Many experimental manipulations change the eAP waveform, either by modulating intrinsic behavior of ion channels underlying transmembrane conductances or by directly targeting the ion channels active during action potentials. Spike sorting routines which cluster eAPs on the basis of shape are challenged by common experimental manipulations that produce changes in the waveform shape, leading to failures in correctly identifying eAPs from the same neuronal source across changing experimental conditions [20]. However, because our method of isolating spikes only depends on the sequence of propagating eAPs at cohort electrodes it is insensitive to changes in eAP waveform.

Our algorithm isolates eAPs from single neurons between experimental conditions that change eAP waveform shape, as shown by comparing the effects of the K^+ channel antagonist 4-AP (100 μM) on propagating eAP waveforms in different anatomical places

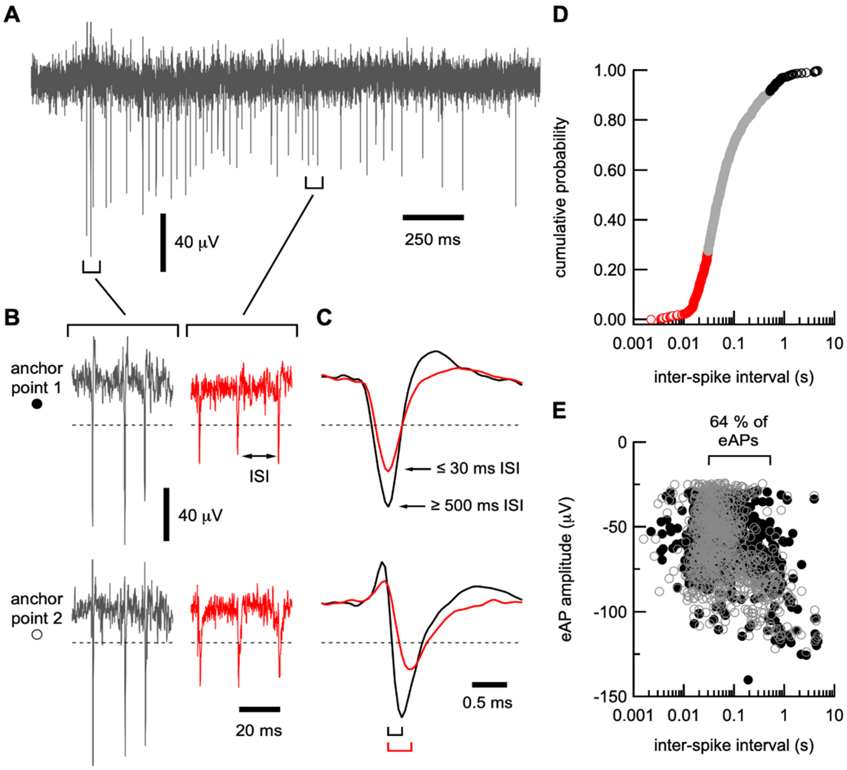

Figure 2.3: Frequency-dependent changes in eAP waveform in single neurons revealed by automated eAP propagation detection. A, voltage record from anchor point 1 electrode showing a frequency-dependent reduction in eAP amplitude. For clarity, only one of two anchor point electrode voltage traces from this propagating eAP is shown here. This burst was preceded by an ISI of > 2 s. B, eAPs in the anchor point 1 and anchor point 2 electrodes, shown at the beginning of the burst (grey traces) and in the middle of the burst (red traces). C, for the propagating eAP from this neuron, we superimposed the average of 50 eAPs that were preceded by ISIs of ≥ 500 ms duration (black traces) on 50 averaged eAPs that were preceded ISIs of ≤ 30 ms. Note the frequency-dependent difference in amplitude and spike width of eAPs from each anchor point electrode. Amplitude scale is the same in B and C. Dashed lines in B and C indicate the eAP detection threshold for each electrode. The averaged waveforms for anchor point 2 eAPs are time referenced to propagating eAPs from electrode 1. Brackets below the waveforms in C indicate the inter-electrode latency for long (black) and short (red) ISIs. D, the cumulative distribution of ISIs from this neuron show large distribution in time. The eAPs that occurred ≤ 30 ms are shown by open red circles, eAPs that occurred ≥ 500 ms are shown by open black circles. Outside of these spike frequency ranges lies the majority of ISIs (open grey circles). E, the relationship between eAP amplitude and ISI in this neuron, showing that the 64% of eAPs occurred after ISIs between 30 and 500 ms for anchor point 1 (closed circles) and anchor point 2 (open circles). This highlights how eAPs kinetics and spike train data from single neurons can be extracted in spite of the frequency-dependent changes in spike morphology.

from the same neuron (Figure 2.4A). Overlaying control eAPs (black traces) and eAPs in 4-AP (red traces) highlights changes due to K^+ channel antagonism in this cultured neuron. Note the heterogeneous effects of 4-AP on eAP waveforms at different points in the propagation pathway from this neuron, including increased duration (panels 1 and 2), decreased eAP amplitude (panel 3) and reducing the repolarization phase (panels 1 - 4). These results illustrate the difficulty in predicting how any drug will affect eAP waveform. Waveform heterogeneity is likely due to how capacitive and resistive components of the eAP waveform combine and are affected by the extracellular electrical field [36]. Figure 2.4B shows the multimodal amplitude distribution in electrode 4 of the propagating action potential from Figure 2.4A, in control (left) and during 4-AP application (right). The amplitude distribution of the propagating eAPs at electrode 4 are indicated in red. In control condition, eAPs isolated from this neuron constitute 37.3% of the eAPs at this electrode (778/2083) which increased to 49.1% (1278/2604) of the eAPs in 4-AP (in a 3-minute recording). Details of how experimental manipulations affect the spike trains from these neurons are seen in the ISI distributions from these data (Figure 2.4C). Solid lines indicate the ISI for all spikes at electrode 4 and dashed lines indicate the ISI of the propagating eAPs, showing in this example no systematic change in the spike train resulting from 4-AP application (Figure 2.4C).

In another experiment, varying the recording temperature from $30°C$ (black traces) to $38°C$ (red traces) also changed the morphology of propagating eAP waveforms at four constituent electrodes from a single neuron (Figure 2.4D). Higher temperature altered the spike width and amplitude (panel 1, 4) and the capacitive component of the eAP (panel 2). Note the leftward shifts of eAPs at higher temperature (panel 3-4), reflecting faster propagation at higher temperature [37, 38]. Regardless of changes in waveform morphology, our algorithm successfully identified propagating eAPs at the same four constituent electrodes. The amplitude histograms of propagating eAPs at electrode 4

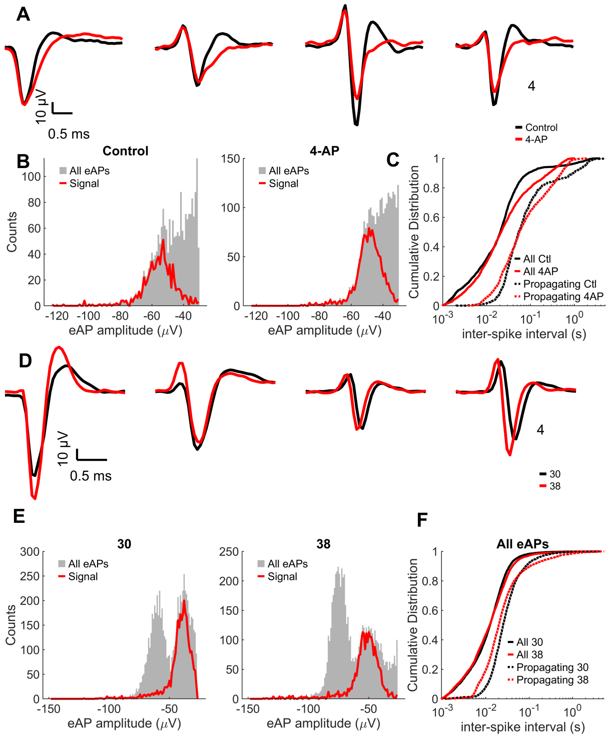

Figure 2.4: Automated detection of eAP propagation during experiments that change eAP waveform. A, the averaged propagating eAP waveforms from four constituent electrodes in control condition (black traces) and in 100 μM 4-AP (red traces) are superimposed, illustrating the effect of 4-AP on eAP waveforms at different points in the propagation pathway. B, single neuron propagating eAP amplitude distribution in control and 4-AP, compared with the all-points amplitude distribution in electrode 4. C, the ISI distribution of all eAPs in electrode 4 versus the ISI distribution of only the propagating eAPs, comparing control and 4-AP. D, in another experiment, the averaged propagating eAP waveforms from 4 constituent electrodes are superimposed to compare waveforms shape in recording at $30°C$ (black traces) versus recording at $38°C$ (red traces). Averaged waveforms for electrodes 2 - 4 are time referenced to electrode 1. Note the leftward shift of the eAP peak in the red traces relative to black, consistent with the temperature induced increase in propagation speed. A and D illustrate that experimentally induced changes in eAP waveform do not affect the ability of our algorithm to detect spikes from the same neuron. E, single neuron propagating eAP amplitude distribution at $30°C$ versus $38°C$, each superimposed on the all-points amplitude distribution in electrode 4. Note the increase in eAP amplitude at higher temperature. F, the ISI distribution of all eAPs in electrode 4 versus the ISI distribution of only the propagating eAPs, comparing $30°C$ and $38°C$. Data in this figure were taken from recordings done on low electrode density arrays (120 electrodes; 100 μm pitch) using cultured mouse hippocampal neurons.

from the temperature experiments (Figure 2.4E) are superimposed on the amplitude histogram of all eAPs at that electrode. For this neuron, propagating eAPs were 42.1% (2849/6768) of all eAPs at electrode 4 at 30°C. Propagating eAPs decreased to 32.9% (2234/6787) of all eAPs at this electrode at 38°C. Propagating eAPs isolated by our algorithm were limited to an apparent single mode of the multimodal, all-point amplitude distributions from these electrodes, even when experimental conditions changed the eAP amplitude distribution (Figure 2.4B, E). Unpredictable changes to the eAP amplitude distributions such as these (Figure 2.4B, E) may result in unreliability of the results of spike sorting. The leftward shift in the ISI distribution from isolated eAPs in this data (red versus black dashed lines) clearly illustrates the effect of higher temperature increases eAP propagation speed (Figure 2.4F). The temperature effect is obscured by overlapping ISI distributions of all spikes in electrode 4 (Figure 2.4F). These results demonstrate that isolating spikes from single neurons based on action potential propagation is insensitive to changes in the eAP waveform and that our algorithm reliably isolates spiking in single identified neurons during changing experimental conditions.

2.1.5 Our algorithm works with multiple extracellular recording platforms

Our algorithm works with any type of multi-electrode spike trains, with no upper limit on the number of electrodes. The time complexity of our algorithm is proportional to:

$$(total\#\, eAPs \times total\#\, electrodes) + total\#\, co - occurrences$$

Multiple propagating eAPs are readily detected with higher density planar CMOS arrays (26,400 electrodes; 17.5 micron pitch). An example of a subset of eAP propagations detected from a 21 x 24 electrode section of CMOS array containing 330 active electrodes, and their footprints generated by signal averaging based on anchor point 1 for each eAP propagation, are shown (Figure 2.5A). For ease of visualization, not all examples of propagating eAPs are displayed. Each waveform represents an electrode from which super-threshold eAP components were recorded (Figure 2.5A). As we've done here, the results of our algorithm could be used for refinement of axonal propagation pathway for each detected signal [31].

Propagating eAPs from single neurons are often detected at multiple electrodes, especially in high-density arrays. The spikes at these electrodes are redundant because a neuron's spiking pattern can be represented by eAPs at anchor point 1. The number of constituent electrodes artifactually multiplies the number of spikes from a neuron. In the case of spike sorting, redundant eAPs such as these could be mistakenly isolated as independent units unless they are removed from the data record. Higher electrode density results in greater number of redundant eAPs; the mean number of cohort electrodes for each eAP propagation on high-density CMOS arrays was 14.1 ± 8.9 electrodes ($n = 1606$ neurons). In contrast, each eAP propagation recorded on low-density arrays was detected by 3.5 ± 2.0 electrodes ($n = 750$ neurons), demonstrating that the extent of the spike redundancy of propagating eAPs varies with recording platform and electrode density. To demonstrate this explicitly, we removed propagating eAPs from all cohort electrodes except for anchor point 1 in multiple recordings from both platform types and plotted the distribution of the percentage of spikes removed from both platforms (Figure 2.5B). In 6/63 recordings using low-density arrays and 33/53 recordings using the high-density arrays, 40% or more of the eAPs in the entire data record could be removed due to redundancy. Similarly, 40/63 of the low-density recordings and 50/53 of the high-density recordings have at least 20% redundant spikes. The relatively high number of cohort electrodes for each eAP propagation in high-density arrays could improve spike train refinement due to more choices for selecting anchor point electrodes with high-signal-to-noise characteristics. These data are from 2-minute-long recordings from low- and high-density arrays. For ease of data acquisition, high-density arrays (26,400 electrodes) were segmented into 32 blocks. Each block was recorded independently because only 1024 electrodes can be recorded simultaneously. This produced 53 recordings from high-density arrays with at least 1 example of eAP propagations, which we compared to 63 recordings in low-density arrays. In arrays with addressable electrodes, our algorithm maximizes the recording efficiency by identifying anchor points for individual neurons. Simultaneous recording of multiple ground-truth validated neurons can then be done in subsequent experiments using the minimum number of electrodes needed to isolate propagation eAPs for each neuron.

We compared the computational time required for our algorithm to output results from the low- or high-density arrays described above (Figure 2.5C). The specification of the server on which this analysis was done is described in Methodology. For a recording with 100000 spikes, the approximate computational time was 3.5 seconds for the low-density arrays we used, and 11 seconds for our high-density arrays. In general, with the same number of spikes, the computational time on a low-density array is less than on a high-density array. This is due to the increase in pairwise electrode comparisons with increasing electrode numbers.

We have shown that eAP propagation can be detected from neurons grown on planar arrays. The three dimensional orientation of axonal process in intact tissue theoretically makes detection of action potential propagation less likely. We examined whether our algorithm could be used to detect propagation in recordings done on a whole cerebral organoid, using a Neuropixels probe. We identified 15 unique neurons based on automated detection of eAP propagation from a Neuropixels recording of 384 electrodes. An example of an eAP propagation detected is shown in Figure 2.5D. The footprint of the eAP propagation was generated by signal averaging based on anchor point 1. Figure 2.5E

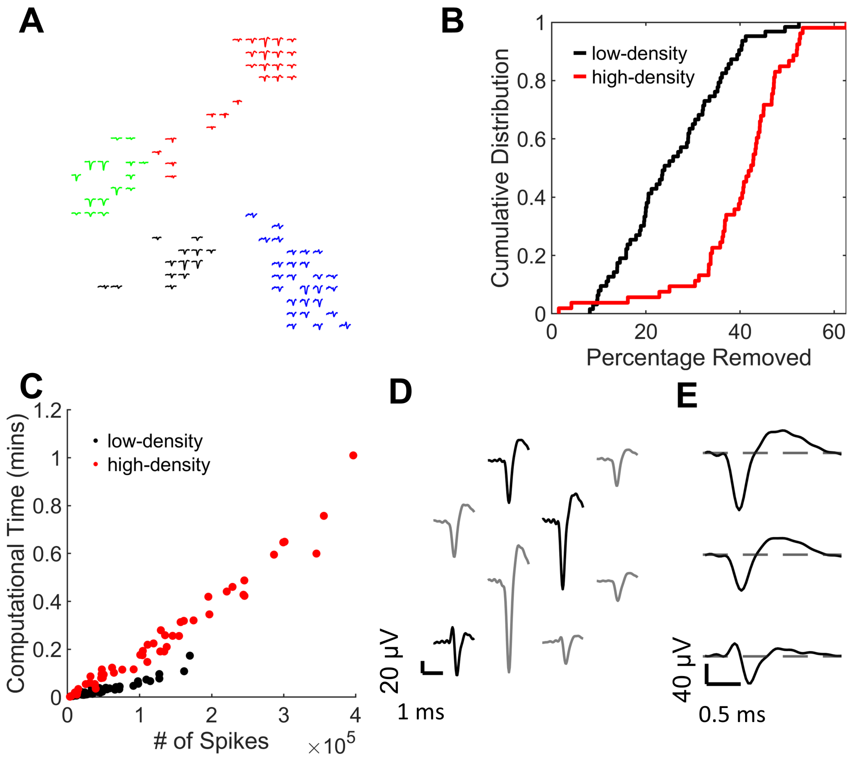

Figure 2.5: Automated detection of eAP propagation handles data from a range of recording platforms. A, a subset of eAP propagations detected on the CMOS array (26,400 electrodes, 17.5 μm pitch). Each color is the footprint of propagating eAPs in one neuron on this 21 electrode by 24 electrode section, with 330 active electrodes. Each footprint is generated by signal averaging based on anchor point 1 for propagating eAPs in each neuron. B, The percentage of 'redundant' spikes eliminated in each recording from low density arrays (black) or CMOS arrays (red). C, Computational time of the algorithm versus the number of spikes with the data from 63 low-density recordings (black) and 53 high-density recordings (red). D, A footprint of an eAP propagation detected on a Neuropixels recording. The footprint is generated by signal averaging based on anchor point 1 for each propagating eAPs. Black lines are the same waveforms shown in (E). Note the time offset from top to bottom in (E), indicating propagation among the three electrodes in three-dimensional tissue from this organoid. Low density arrays have 120 electrodes with a 100 μm pitch. High density CMOS arrays have 26,400 electrodes with a 17.5 μm pitch. Recordings on low and high density arrays were done using cultured mouse hippocampal neurons. The Neuropixels probe was used to record eAPs from a cerebral organoid derived from human iPS cells.

shows the same waveforms from the ones in black in Figure 2.5D. Note the time offset from top to bottom from these electrodes. These data demonstrate that with high density arrays, isolating eAPs from single identified neurons in 3 dimensional neural tissue is possible with automated detection of action potential propagation.

2.2 Methodology

2.2.1 Propagating eAP detection algorithm

The input of the algorithm is spike times on all electrodes in a recording. The first step in our algorithm is to select candidate electrodes that could be cohort electrodes of an eAP propagation. Let E denote the total set of electrodes in an array and n denote the total number of electrodes in E. Each electrode in E with an average spiking frequency higher than v_1 Hz is used as a reference electrode (e_i) to compare with all other electrodes $e_j \in E$ (j = 1, 2, . . . , n). This threshold value for spiking frequency v_1 ensures a minimum number of spikes on each reference electrode for the analysis in the next steps. v_1 is a user-definable parameter. In this paper, we chose v_1 to be 1Hz. We used this frequency threshold because most of our recordings were 2- or 3-minutes duration. In longer recordings, v_1 can be adjusted to a lower value. We also included an option to threshold for the minimum number of spikes in total instead of the spiking frequency.

Cross-correlograms (CCGs) using a 1.5 ms window before and after reference timepoints with a bin size of 0.05 ms were then constructed for all (e_i, e_j) pairs. A sharp peak in a CCG indicates a strong correlation of spike times between e_i and e_j. To quantify sharp peaks, let n_1 denote the largest sum of counts in any 0.5 ms moving window in the CCG and n_2 denote the sum of counts of a 2.05 ms window centered at the bin with the largest sum (if the largest sum is found in the first 1 ms or the last 1 ms of the CCG, take the sum of the counts of the first 2.05 ms window or the counts of the last 2.05 ms window as n_2). The bigger the ratio n_2/n_1 is, the sharper the peak is. A customizable variable v_2 is used to threshold the lower bound of the ratio. An empty list is created for each e_i. When the ratio n_2/n_1 for an (e_i, e_j) pair is larger than v_2, we add e_j to the corresponding list for e_i and record the lag in the CCG bin with the largest number of counts as the delay time of e_j relative to e_i. After the list is constructed, for each e_i, if all e_j in the list have non-negative delay times, we store this list as a set of candidate electrodes for a propagation. The requirement for non-negative delay times for all e_j avoids duplicate detection of the same eAP propagation. This process is repeated for all electrodes e_i in an array. In this paper, we chose v_2 to be 0.5. The value 0.5 was determined empirically with results from different thresholds compared with manually detected propagation signals for our dataset as described in [22]. Users can change v_2 to any number between 0 to 1 based on how sharp they want the peaks for a qualified electrode pair to be.

After a set of candidate electrodes is found for a reference electrode e_i, the second step is as follows. First, find the electrode e_h in the set of candidate electrodes with the maximum number of co-occurrences with e_i. If there are multiple electrodes with the same number of co-occurrences with e_i, the one with a shorter delay time is identified as e_h. If there are multiple electrodes with the same number of occurrences with e_i and the same delay time, the one with a smaller ID number is used as e_h. Second, scan through all other electrodes in the set of candidate electrodes to identify only the electrodes with more than $v_3\%$ of the maximum number of co-occurrences and an n_1 greater than v_4 (n_1 denotes the largest sum of counts in any 0.5 ms moving window in the CCG). Action potential propagation is a high-fidelity process where ideally, all cohort electrodes detect most of the propagating eAPs. In practice, missed spike detection happens in electrodes with low signal-to-noise ratio. v_3 is used as the threshold for the lower bound of the percentage of co-occurrences each cohort electrode needs to detect for an eAP propagation. Given the low inter-electrode latency variability, n_1 is a proxy of the absolute number of co-occurrences. Co-occurrences can happen from random alignment. However, we showed in Figure 2.2G and 2.2H that random alignment only leads to a small number of co-occurrences. The threshold v_4 sets a lower bound for the number of co-occurrences to avoid falsely identifying an electrode as a cohort electrode as a result of random alignment.

In this paper, we used $v_3 = 50$ and $v_4 = 50$. v_3 was determined empirically with results from different values compared with manually detected propagation signals for our datasets as described in [22]. We chose v_4 to be 50 based on the number of spikes in each recording. Electrodes that satisfy these criteria along with e_i, e_h are identified as the cohort electrodes of an eAP propagation. This process was repeated for all sets of candidate electrodes. This generates a collection of cohort electrodes, each representing an eAP propagation in each recording.

All v_i can be defined by users.

2.2.2 Signal statistics extraction

The eAPs from the identified cohort electrodes can be used to extract single cell statistics. Spike times T_i for an identified neuronal source s_i are computed using the spike times on the cohort electrodes. Let e_i again denote the reference electrode in the cohort and eh denote the electrode with the most co-occurrences with e_i. Here co-occurrences were spikes at cohort electrodes that occurred within 1.5 ms window following the eAP at the reference electrode. e_i and eh are the first two anchor points for s_i. First, all the co-occurrences between these two anchor points are identified and added to a spike set S.

Additional anchor points can be added in the order of most to least co-occurrences with anchor point 1. The co-occurrences between the additional anchor point with anchor point 1 are added to S to comprise an amended set of propagating eAPs. Note that because inter-electrode latencies are usually small (<1 ms), we use the spike times at anchor point 1 to represent the spike times of the neuronal sources.

In this work, the propagation eAPs were isolated with three anchor points when possible, unless otherwise specified. In cases with only two cohort electrodes, the propagation eAPs were isolated with two anchor points.

The analysis for computational time in Figure 2.5C was done on a server with the following specifications: Chassis: Gigabyte R282-Z91-00 Rack Mount Server; Motherboard: Gigabyte MZ92-FS0-00; CPUs: two AMD EPYC 2 Rome 7502 32 Core CPUs; RAM: 1TB DDR4 Reg ECC RAM; Operating System: Ubuntu 20.04 LTS. The software used to run the script was MATLAB R2018b. The code used parfor (parallel) for-loops and employed 12 workers on the server for parallel computing.

2.2.3 Primary cell culture

All animal protocols and procedures described in this study were approved by the Institutional Animal Care and Use Committee (IACUC) of University of California, Santa Barbara and were performed in accordance with the NIH Health Guide for the Care and the Use of Laboratory Animals. All animal experiments were performed in accordance with ARRIVE guidelines. Primary hippocampal neurons were isolated from postnatal day 0 (P0) C57BL/6 mice using previously described protocols. Up to 3 mouse pups were used per round of cell culture and the neurons were pooled for plating on multiple MEAs. Cleaned and UV sterilized MEAs (120MEA100/30iR-ITO arrays; Multi Channel Systems) were coated with 0.1 mg/ml poly-L-lysine (Sigma-Aldrich) for 1 h at 37 $^{\circ}C$, rinsed 3 times with sterile water and air dried prior to plating. All recordings were done from cultures that were plated twice. In the first plating, primary cells were plated and allowed to grow and proliferate. After at least a week, another round of primary cells was plated. Cells were plated at 100,000 to 125,000 cells for the first plating and 125,000 to 200,000 for the second plating. For cultures grown on CMOS arrays, cultures of primary glial cells were maintained in separate T-75 flasks, were plated at 150,000 cells per well on MEAs and allowed to proliferate for at least a week. Freshly dissociated hippocampal cells were then plated at 250,000 cells per dish (550 cells/mm^2) on the confluent glial cultures. All primary mouse cultures were grown in minimum essential medium with Earle's salts (Thermo Scientific, catalog # 11090081) with 2 mM Glutamax (Thermo Scientific), 5% heat-inactivated fetal bovine serum (Thermo Scientific), and 1 ml/l Mito+serum extender (Corning) and supplemented with glucose to an added concentration of 21 mM.

2.2.4 Human brain cerebral organoid generation

Details on generation of the cerebral brain organoids have been previously published [39]. The control induced pluripotent stem cell (iPSC) line F12442.453 were cultured in mTeSR1 medium (Stem Cell Technologies) using hESC-qualified Matrigel-coated tissue culture plates (Corning). Media was exchanged every other day and iPSCs were routinely passed using ReLeSR (Stem Cell Technologies). Organoids were generated using the method of [40], with minor modifications. For dissociation, iPSCs were incubated in 0.5 mM EDTA in D-PBS for 3 min followed by Accutase for 3 min at 37 $^{\circ}C$ and triturated to achieve a single-cell suspension. Cells were centrifuged for 3 minutes at 1,000 rpm, resuspended in low bFGF hES media supplemented with Rock inhibitor (50 μM) and plated in U-bottom ultra-low attachment plates at 4,500 cells per well. On day 2, low bFGS hES media with Rock inhibitor was replaced. Media was changed on day 4, omitting bFGF and Rock inhibitor. Embryoid bodies were transferred to neural induction media on day 5 (1x N2 supplement, 1x GlutaMAX, 1x MEM-NEAA, 1ug/ml Heparin in DMEM/F12) and media was replaced on days 7 and 9. On day 10, each neuroepithelial structure was embedded in 15 ul hESC-qualified Matrigel, followed by a 2 day incubation in neural induction media. On day 12, neural induction media was replaced with NeuroDMEM-A media (0.5x N2 supplement, 1x B27supplement without Vitamin A, 1x β-Mercaptoethanol, 1x GlutaMAX, 0.5x MEM-NEAA, 250 ul/l insulin solution, 1x Pen/Strep in 50% DMEM/F12 and 50% Neurobasal). After day 19, organoids were cultured in NeuroDMEM+A media (0.5x N2 supplement, 1x B27 supplement with Vitamin A, 1x β-Mercaptoethanol, 1x GlutaMAX, 0.5x MEM-NEAA, 250 ul/l insulin solution, 12.5 mM HEPES, 0.4 mM Vitamin C, 1x Pen/Strep in 50% DMEM/F12 and 50% Neurobasal) with media changes twice per week. After day 21, organoid cultures were kept on an orbital shaker at 75 rpm.

2.2.5 Recording conditions

All recordings from low density arrays (MultiChannel Systems; Reutlinger, Germany) or CMOS arrays (Maxwell Biosystems; Zurich, Switzerland) were done in cell culture medium to maintain sterility (see above). Low density arrays (100 micron inter-electrode distance) were recorded using MultiChannel Systems MEA 2100 acquisition system. Data were acquired at 20 kHz and post-acquisition bandpass filtered between 200 and 4000 Hz. Data were acquired on all 120 data channels. We controlled the head stage temperature with an external temperature controller (MultiChannel Systems TC01). Most recordings reported here were done at $30°C$, unless otherwise indicated. The media osmolality was usually $\sim$320 mosmol. Salts were obtained from Sigma-Aldrich or Fluka. Any drugs, such as TTX (Tocris), were introduced into the recording chamber in a volume not more than 0.2% of the chamber volume.

All recordings were done on neurons at 5-30 days in vitro (DIV) except for recordings done on organoids. We used recordings with signals present on the majority of channels. Recording duration was kept brief (3 to 5 minutes) to minimize to avoid large changes in CO_2 and pH [22] and to minimize data file size. All recordings were done with the MEAs chambers covered by a CO_2-permeable, water vapor-impermeable membrane to minimize evaporation, maintain cell culture sterility and decrease media degassing. Membranes were held in place over the recording chamber by a Teflon collar placed over the culture chamber. Once placed in the headstage, each array was allowed to equilibrate to head stage temperature for at least 5 minutes. For experiments requiring temperature changes, head stage temperature was monitored and each MEA was kept at the new temperature for at least 5 minutes before data acquisition. For all CMOS recordings, the headstage was kept in a cell culture incubator equilibrated to 5% CO_2 and 37 °C. CMOS data were acquired at 20 kHz. Data were acquired on a subset (1024 electrodes) of the 26,400 available electrodes.

Recordings from cerebral organoids were performed using a high-density Neuropixels CMOS shank (Neuropixels, Heverlee, Belgium) on 6-month-old cerebral organoids. Briefly, organoids were cultured in BrainPhys media for 30 days prior to recording. For recordings, organoids in BrainPhys media were immobilized in a custom well and kept at 37 $°C$ using a temperature-controlled stage. A 10 mm long high-density Neuropixels CMOS shank (with 384 addressable electrodes in 960 electrode array) was inserted into the organoid using a motorized micromanipulator (MP-285, Sutter Instruments). Data acquisition was done with SpikeGLX (Bill Karsh, https://github.com/billkarsh/SpikeGLX) at a sampling rate of 30 kHz. Subsequent data processing and analysis were performed similarly to 2D CMOS data.

2.2.6 Spike detection and analysis

MultiChannel Systems proprietary files were converted to HDF5 file format prior to all analysis with the MCS program Multi Channel DataManager. Extracellular voltage records were bandpass filtered using a digital 2nd order Butterworth filter with cutoff frequencies of 0.2 and 4 kHz. Spikes recorded from the MultiChannel Systems acquisition system were detected with MEA Tools [25] using a threshold of 6 times the standard deviation of the median noise level. For CMOS recordings, raw voltage records were bandpass filtered between 300-6000 Hz and the spike detection threshold was 5 times the root mean squared of the signal per channel. Raw data was processed using proprietary MaxLab Live software (Maxwell Biosystems). Manually detected propagating eAPs were initially detected by eye with the help of MEA Viewer [25] spike visualization software and validated by signal averaging. No spike sorted data was used in our analysis. Some analysis was done using custom software written in Python and Mathematica (Wolfram) and in Igor (Wavemetrics). For example, to compare the output of our detection algorithm with raw data (Figure 2.1), output files from MEA Tools containing spike times and amplitudes were manually compared to amplitude histograms from eAPs isolated with our algorithm. All statistical data are displayed as the mean ± standard deviation.

2.3 Discussion

2.3.1 Limitations of automated detection of action potential propagation

Since the method we outline here uses action potential propagation to isolate eAPs from individual neurons, a minimum of two electrodes are required for propagation detection. Propagation from some neurons may be undetectable due to their axons being outside the detection radius of any electrode. This is especially true for lower electrode density arrays. However, denser arrays of electrodes will result in increased detection of propagation. In the case of high electrode density arrays implanted in the human brain organoid (Figure 2.5D, 2.5E), the blind insertion of the shank array and the unknown cellular anatomy likely contributed to the limited detection of propagating action potentials. With respect to the in vivo application of our algorithm, detection of propagating eAPs may be facilitated in experiments where shank electrode arrays are inserted parallel to fiber tracts in white matter, for example.

The input of our algorithm is spike trains that have been detected by other means. Sampling the true spike train from any neuron is always limited to signal-to-noise considerations. Our algorithm depends on co-detection of eAPs at two cohort electrodes and therefore increases the risk of under-sampling the true spike train when the signal-to-noise ratio at any anchor point is low. Because our algorithm always uses the cohort electrode with the earliest eAPs in the propagation sequence as anchor point 1 and indexes the propagating eAPs at all other cohort electrodes to the earliest eAPs, detection accuracy is limited by the signal-to-noise at this electrode. The earliest electrode often includes eAPs with waveforms consistent with them arising from at or near the axon initial segment (AIS; Figure 2.1B, 2.4A, 2.4D). Because the transmembrane conductance at the AIS is large[41, 31], the signal-to-noise of these eAPs is typically quite high. However, propagation detection is compromised the lower the signal-to-noise ratio is of other cohort electrodes (Figure 2.2C).

We circumvented some signal-to-noise limitations of spike detection by designing into our algorithm a user-defined option to include spike trains from cohort electrodes other than anchor points 1 and 2 (Figure 2.2). Detection failures at the anchor point 2 electrode could be compensated for by increasing the number of electrodes for propagation detection. Doing so revealed more propagating spikes (Figure 2.2E, F). However, using propagating eAPs from other cohort electrodes refines the spike train (Figure 2.2E) but the increased comparisons between spikes increases the risk of false positives due to random alignment (Figure 2.2H).

Repeated co-occurrence of eAPs is the detection criteria for isolating propagating action potentials from different source neurons. Artifactual alignment of spikes that are not reflective of propagation at other electrodes can be mistaken as propagating eAPs.

This concern increases when the spike rate at any electrode is high. However, as we show (Figures 2.1D, 2.2G, 2.2H), the number of artifactually isolated propagating eAPs due to randomness was minimal under our recording conditions. Propagating eAP detection can be affected by additional thresholding based on the standard deviation of inter-electrode latencies which gives rise to the CCG. Propagating action potentials have low variability of the inter-electrode latency. Thus, eAPs at other electrodes with latencies that are at the edges of the latency distribution are more likely to represent noise. Figure 2.6 displays an example of additional thresholding based on the standard deviation of inter-electrode latency. Each panel shows the amplitude distribution of all eAPs at an electrode (in grey) superimposed with the amplitude distribution of propagating eAPs (red) isolated using different thresholding. The first three panels display how thresholding, based on different multiples of the standard deviation (α), affect the isolation of propagating eAPs. The final panel shows the isolated propagating eAPs amplitude distribution without any such thresholding. The amplitude distribution at this example electrode is divided into two modes; we expect the propagating eAPs to be limited to an apparent single mode. However, a small number of spikes from the lower amplitude mode were included by the algorithm. With different value of α, different number of eAPs were removed. Without thresholding, there are 1939 propagating eAPs in the higher amplitude mode and 139 propagating eAPs in the lower amplitude mode. When threshold was set to $\alpha = 2$, 90% of the eAPs in the lower amplitude mode were filtered out while retaining all of the eAPs in the higher amplitude mode. In general, smaller α will filter out some true co-occurrences and cause higher false negative rate whereas a larger α can cause higher false positive rate.

Signal quality affects propagation detection in other ways. For example, our algorithm uses parameters such as the shape of the CCG and the number of propagating eAP co-occurrences (see Methodology) to identify cohort electrodes. When detection failure varies between recordings, such as during experimentally induced changes in propagating eAP waveforms (Figures 2.3, 2.4), these parameters can be affected and can result in identification of propagating eAPs with different numbers of cohort electrodes. However, the majority of spike train data from propagating eAPs in each neuron is usually represented by 2 to 3 electrodes (Figure 2.2I, J), within the limits of detection. Analytically, this outcome matters, for example, when trying to increase the anatomical detail of the propagation pathway. Changing the spike detection threshold could reveal such cases.

2.3.2 Future Directions - complementary use with traditional spike sorting routines

Use of contemporary MEAs requires automated approaches for post-acquisition data handling, due to the large number of sensors that each acquire data at the high enough acquisition rates to represent eAPs. To understand how any experimental manipulation affects spike rate, extracellular recording on the scale possible with contemporary MEAs requires automated methods of isolating spikes into different sources. However, sorting routines that are untested against contextually relevant ground truth could produce erroneous results in the absence of other information. In the absence of ground truth, even the most sophisticated sorting routines are unable to validate how to correlate spikes at single electrodes in experiments that significantly change the eAP waveform [20]. Our

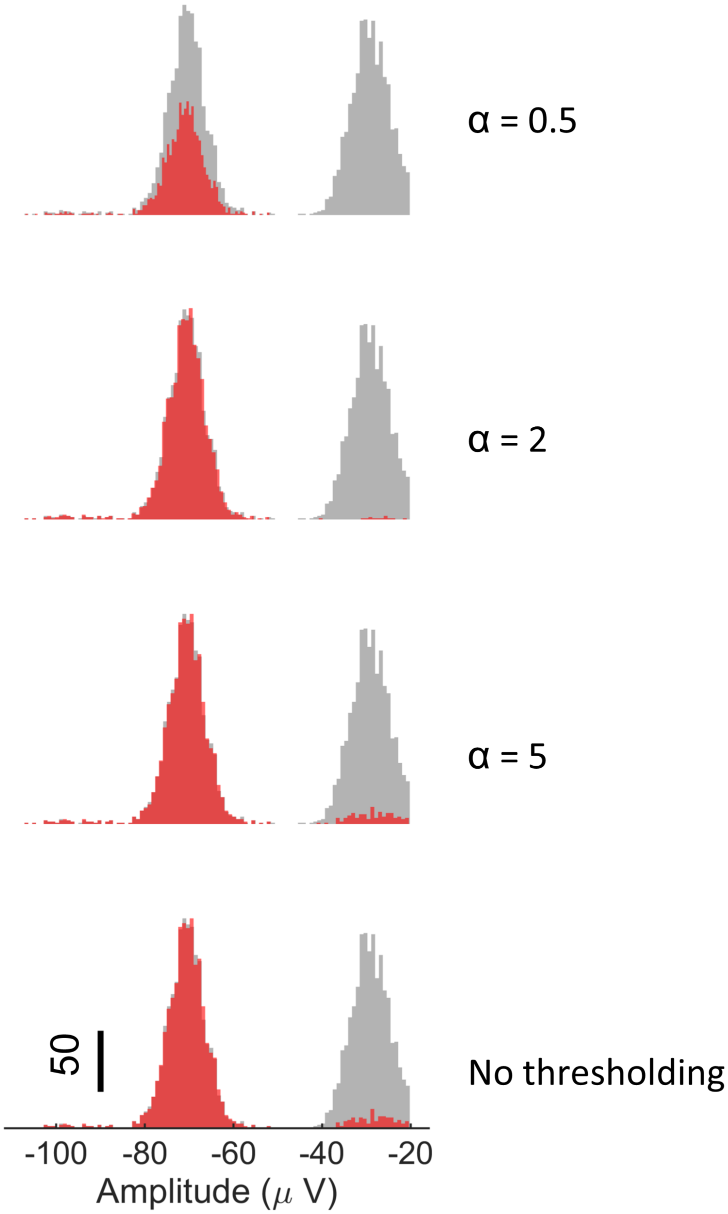

Figure 2.6: An example of the usage of multiples of standard deviation (α) of the latency distribution for thresholding. In each histogram, grey are the amplitudes of all eAPs at this electrode. Superimposed on these histograms are the amplitude distributions of isolated propagating eAPs (red). From top to bottom, the first three histograms show the eAP amplitude distribution after thresholding with $\alpha = 0.5$, $\alpha = 2$ and $\alpha = 5$ respectively. The histogram at the bottom is the propagating eAPs detected without any thresholding.

approach to isolating eAPs from different source neurons based on detection of eAP propagation, routinely provides contextually relevant ground truth and thus could be used to test spike sorting routines in every experiment in which propagation is detected. For example, at each electrode, eAPs assigned to individual units by spike sorting routines could be tested against eAPs at that same electrode that were isolated as part of a propagation cohort. The extent of overlap between results from a sorting routine and the results from our method assesses the accuracy of a sorting routine [22].

Isolation of eAPs by automated detection of action potential propagation performs the same task as traditional spike sorting. The characteristics of action potential propagation themselves validate that eAP cohorts isolated by this method are from individual neuronal sources. Thus all spikes isolated by our method can be ignored by traditional spike sorting routines. However, the characteristics of propagation detection mean that the fraction of spikes in any data set that can be isolated by this method will depend on factors such as electrode and neuron density. For example, densely packed electrodes more readily detect propagation than more widely spaced electrodes (Figure 2.5B). In intact tissue, positioning electrode arrays within fiber tracks or other neuronal propagation pathways should facilitate propagation detection. Data acquisition in the range of experimental contexts in which MEAs are used means that automated detection of action potential propagation and traditional spike sorting routines are complementary. A workflow in which spike train data is processed by our algorithm, followed by a traditional spike sorting method, may reduce the vulnerability of the remaining ensemble spike train to be miss-sorted. This also increases the reliability of eAP isolation of the entire data record because of the empirical isolation of eAPs with our algorithm as the first step.

Sorting eAPs into source neurons based on action potential propagation avoids limitations of waveform-based sorting. Because eAPs are isolated into unique sources based on the propagation pathway rather than waveform, drug development assays based on extracellular recording on high throughput MEA platforms become unconstrained by ambiguity introduced when drug application changes spike waveform [20]. Other experimental manipulations that change eAP waveforms can also be unambiguously studied with the implementation of our algorithm because the response of each identified neuron can be tracked among various conditions. When eAPs are unambiguously assigned to a unique neuronal source, those eAP times are an index against which eAPs from other neurons can be timed, for example to identify synaptic coupling among small numbers of neurons [24] or to assess how genetic background affects synaptic coupling, for example. Further development of our methods can start to bridge the gap between rapidly evolving MEA technology and science that use of such technology can reveal.

Chapter 3

Extracellular detection of neuronal coupling

3.1 Results

3.1.1 Propagating eAPs are a timing device

We isolated eAPs from single identified neurons by extracting action potential propagation signals from single axons across multiple electrodes[22, 42]. We previously characterized axonal action potential propagation by isolating cohorts of electrodes with eAPs that occur in fixed spatial and temporal relationships[22] as a means to identify and label each individual isolated neuron. For example, spikes between electrodes H6 and D6 (Fig. 3.1a, b) co-occurred 1360 times in this recording, with an inter-electrode latency of 0.305 ± 0.024 ms and a coefficient of variation (CV) of 0.078, consistent with a high-fidelity process like axonal action potential propagation. Isolation of eAP propagation signals within the multi-electrode voltage record in this way empirically reveals spiking from single neurons.

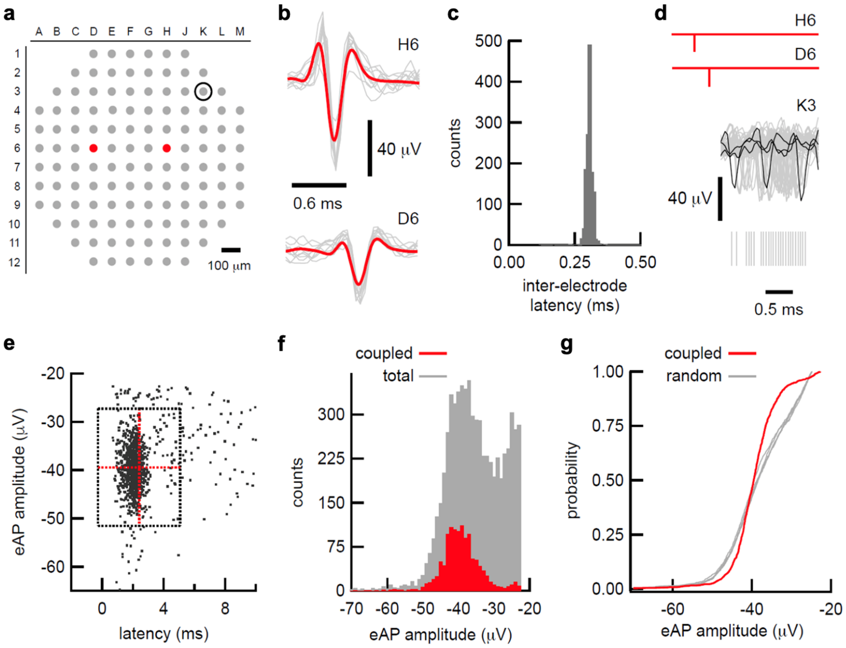

Figure 3.1: Propagation signals are a clock used to identify coupled eAP's. a, Map of electrode array used in these experiments. Two electrodes that detect single axon eAP propagation are shown in red. Electrode K3 is the location of the spike cloud that follows the propagation signal. b, The eAP waveforms at H6 and D6 are shown. Individual eAPs are in grey; the average of 100 eAP waveforms is superimposed in red. c, The distribution of inter-electrode eAP latency between H6 and D6. The high number of co-occurrences (n = 1360) and low coefficient of variation (0.078) are consistent with action potential propagation. d, aligning the eAP co-occurrences at H6 and D6 (schematized in red) reveals a cloud of eAPs at K3. Twenty eAP waveforms from K3 are superimposed in grey, with 3 waveforms highlighted in black. The timing of 50 eAPs from K3 following the H6/D6 co-occurrence are shown as grey hash marks beneath eAP the waveforms. e, the plot of eAP amplitude at versus time after H6/D6 co-occurrence shows a large cluster. All eAPs that occurred between 0.5 and 10 milliseconds after the H6/D6 co-occurrence are displayed. Red lines indicate the mean latency and eAP amplitude, respectively. Horizontal and vertical grey lines indicate two standard deviations of the mean for each dimension. f, the amplitude distribution of the spikes in K3 that occurred within 0.5 to 10 ms following the H6/D6 co-occurrence (red bars) are superimposed on the all-points spike amplitude distribution histograms from electrode K3. g, cumulative distribution of the coupled spikes in K3 (red line) superimposed on the cumulative distributions from 5 randomly selected groups of amplitudes from the all-points distribution from K3, showing that the amplitudes of the coupled eAPs were not randomly selected from the full amplitude distribution.

The co-detection of action potentials by multiple electrodes was the time stamp we used to mark events at other array electrodes. Because co-occurrences represent spiking from a single neuron, we can recalibrate the timing of all other electrodes by indexing the voltage record to the co-occurring eAPs. Superimposing the co-occurring spikes from each unique propagation signal recalibrates the timing of other eAPs with relation to the timing of the propagating events. For example, superimposing co-occurring spikes from H6 and D6 (Fig. 3.1c) revealed a cluster of spikes at another electrode (K3) that occur with short, variable latency after the propagating spikes (Fig. 3.1d). In this example, spikes in K3 occurred with a probability of 0.85 between 0.5 to 10 milliseconds after the propagating eAPs, with a latency of 2.40 ± 1.33 ms (n = 1205; Fig. 3.1e). The latency CV of these coupled spikes (0.55) is inconsistent with action potential propagation while the high probability and short latencies of eAPs in K3 suggested direct coupling of spiking between the propagation signal neuron and a neuron detected at electrode K3.

Extracellular electrodes can detect spikes from any sufficiently proximal neuron. Consequently, the eAP amplitude distribution of single electrodes can reflect spikes from multiple source neurons[43]; spike amplitude can often be discriminating criteria in spike sorting routines[12, 44]. The full eAP amplitude distribution from electrode K3 is multimodal, potentially representing spikes from at least two source neurons (Fig. 3.1f, grey bars). In contrast, the amplitude distribution of the eAPs at K3 that occurred between 0.5 to 10 milliseconds after propagation signal H6/D6 was a discrete subset of the entire eAP amplitude distribution rather than a randomly sampled subset of the full amplitude distribution (Fig. 3.1f, red bars). To formally examine if the amplitude distribution of coupled spikes at K3 could be explained by random selection from the entire amplitude histogram, we compared the amplitude distribution of the eAPs coupled to the propagation H6/D6 to the amplitude distributions of multiple randomly sampled eAPs amplitudes from K3, using the Kolmogorov-Smirnov (KS) test, which tests the probability that groups of spikes were taken from the same distribution (Fig. 3.1g). The probability that the distribution of coupled eAPs and randomly sampled eAPs were from the same distribution was less than 1.0×10^{-14} (two-sample KS test, two-sided, $n = 1205$). In contrast, the probability that two randomly chosen groups of eAPs from electrode K3 were drawn from the same amplitude distribution was 0.64. These results suggest that eAPs from a single source neuron occur with short latency after the propagating spike H3/E6. Our results further suggest the short latency between eAPs from the neuronal source of the propagation signal eAPs and downstream clusters of spikes reflects direct synaptic coupling.

3.1.2 Detection of neuronal coupling with an automated detection algorithm

To apply the high throughput capabilities of MEAs efficiently, we developed algorithms for the automated detection of (1) propagation signals and (2) neurons with short latency couplings based on clusters of post-synaptic eAPs. We first isolated eAPs from single neurons, using all 120 electrodes to detect propagation signals. We then used the propagation signal spike times to create cross-correlograms (CCGs), with a 2 ms window before and after reference time-points for each pair of eAP spike time comparisons among all electrodes. The process was repeated for all array electrodes, generating a collection of all propagation signals with the delay time of the electrodes through which they pass (Fig. 3.2a).

The spike times of each propagation signal were then used as reference time-points for detection of short-latency connections between propagation signal spike times and eAPs at all other electrodes. A new CCG was performed for each pair of comparisons, using a window between 0.5 and 10ms after each reference time-point (Fig. 3.2b) with

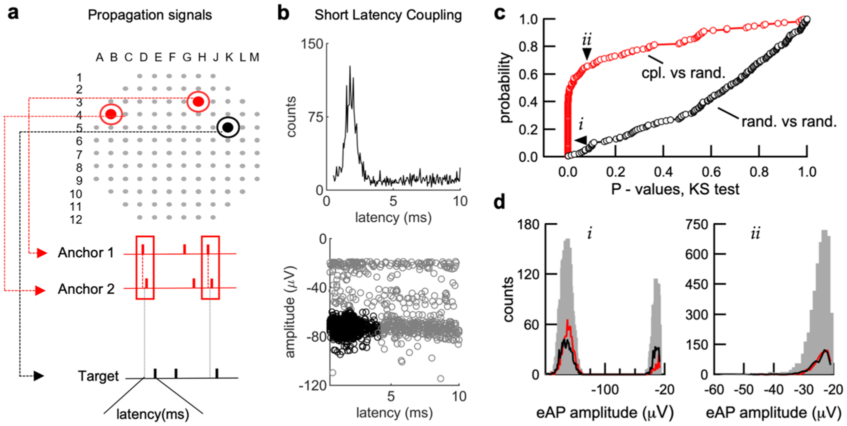

Figure 3.2: Algorithm for the routine detection of synaptic coupling. a, following propagation signal detection, two electrodes with the most co-occurrences from each propagation signal were picked as anchor points to compute the spike times. b, A CCG is generated and stored using propagation signal spike times as a reference and all other individual electrodes as targets. To inspect the specificity of the postsynaptic response, a scatter plot of spike amplitude versus spike latency in the target electrode is produced. A few criteria can be used for deciding the existence of a short latency connection including: 1) The position of the peak of the CCGs, 2) the standard deviation of the latency and amplitude, 3) the proportion of spikes that fall into the peak region, and 4) the ratio of the number of spikes in the peak region to the number of spikes in the reference signal. The specific values for the criteria can alternatively be user defined. c, d (right) The two-sample KS test (two-sided) p - value distribution of coupled-versus-coupled comparisons (red circles) and random-versus-random comparisons (black circles). The amplitude distributions of some electrodes are expected to be unimodal if eAPs from only single neurons are detected by those electrodes. In these cases, coupled spikes would be expected to have the same amplitude distribution as randomly selected spikes, as is the case for comparisons that do not differ.

filtering criteria described in the Methodology section. The coupling probability is the ratio of spikes in the CCG peak over the total number of propagation signal spikes.

To test whether our algorithms were randomly selecting eAPs from each electrode, we used the two-tailed KS test to determine the probability that coupled spikes were selected from the same amplitude distribution as a randomly selected group of spikes from the entire distribution of the same electrode. We also compared two groups of randomly selected eAPs from the same electrode to test the probability that they were from the same distribution. As seen, most (94/156) of the coupled-versus-random comparisons (red circles) were unlikely to have been selected from the same distribution at a 5% significance threshold (Fig. 3.2c). In contrast, 152 of the random-versus-random comparisons (black circles) exceeded this threshold. These data indicate that the coupled spikes selected by our algorithm are a non-random selection from the full eAP amplitude histogram at each electrode.

The amplitude distribution of coupled spikes (red lines) selected by our algorithm in this example (Fig. 3.2d, left) are predominantly sampled from the higher amplitude mode of the full distribution (grey bars). In contrast, the randomly drawn sample of eAP amplitudes (black line) mirrors the full amplitude distribution. This difference led to a low probability ($P < 6.7 \times 10^{-35}$) that coupled spikes and randomly selected spikes were drawn from the same sample. However, in some cases, such as when only one neuron is proximal to an electrode, the amplitude distribution will approximate a normal distribution. Thus, when we apply our algorithm under these circumstances, the coupled spike amplitude distribution will be indistinguishable from a randomly selected group of spikes (Fig. 3.2d, right). In cases where electrodes sample from multiple neurons, coupled spikes extracted by our algorithm represent a statistically distinct subset of the full events, consistent with eAPs from single neurons and with statistical characteristics outlined previously (Fig. 3.1f, g). To examine whether our results arose because of random associations between pre- and postsynaptic neurons, we shuffled the timing of all spikes at postsynaptic electrodes, while retaining the distribution of inter-spike intervals (ISI) for each electrode and calculated the ratio of the number of spikes in the target electrode that fall within 0.5 to 10 ms of a spike in the reference electrode over the number of spikes in the reference electrode signal. We found that the ratio dropped from 0.35 ± 0.25 in unshuffled controls to 0.0035 ± 0.0038 in the shuffled data (n = 746 detected couplings), indicating that what our algorithm identified as couplings were not the result of the randomness of timing associations between spikes at different electrodes. Our results indicate that our algorithm detects spikes that are postsynaptic to the propagation signal eAP, likely representing examples of synaptically-coupled neurons from the extracellular voltage record.

3.1.3 Stimulation recapitulates properties of spontaneously-coupled spikes

The majority of eAPs in our cultures result, directly or indirectly, from excitatory synaptic transmission. Blocking excitatory neurotransmitter receptors in our cultures (2.5 – 5 μM NBQX and 10 μM R-CPP) reduced the number of spikes to 12.5 ± 15.2% of control (n = 7 arrays). The latency between propagation signal eAPs and coupled spikes suggests a direct synaptic interaction. We tested whether we could recapitulate the coupling probability of spontaneously active neurons by direct stimulation of the propagation signal neurons. In this example, the coupled eAPs at electrode A7 (Fig. 3.3a) consistently and closely followed the propagation signal D3/E5, with a probability of 0.65 (n = 377 coupled spikes). If eAPs from the propagation signal D3/E5 result in spikes at A7, stimulation of electrode D3 should result in eAPs that occur with a similar probability and amplitude distribution at A7. As shown, stimulation resulted in eAPs in

A7 with a probability of 0.79 (n = 393 coupled spikes; Fig. 3.3a). The spike amplitudes at A7 following spontaneous propagation signals (44.14 ± 9.15 μV) or stimulation (44.75 ± 14.17 μV) did not differ (n = 200 randomly chosen spikes from each group; P = 0.2; two-sample KS test, two-sided; Fig. 3.3b). The latency of the coupled spikes was 4.29 ± 0.69 ms in the spontaneous conditions and 5.93 ± 0.63 ms in the stimulated condition. For stimulation, the latency was the interval between the beginning of the blanking period and the negative peak of the coupled spike. The longer latency following stimulation likely reflects the difference in how latency was measured in these cases. This suggests that spontaneous eAPs at A7 following the propagation signal or the stimulation of the propagation signal are from the same source neuron.

Across multiple experiments, the coupling probability between spontaneous and stimulated cases were comparable, as shown by plotting coupling probability for spontaneous events as a function of coupling probability for evoked events (Fig. 3.3c). The slope of the linear fit to this data was 0.84 (n = 20). A paired t-test (two-sided) showed no significant difference when comparing coupling probability for spontaneous and evoked cases (P = 0.45). Similarly, a plot of the mean amplitude of spontaneous eAPs as a function of the amplitude of evoked eAPs was well fitted to a line with a slope of 0.93; the amplitudes of coupled spikes following stimulation were not statistically different from those of spontaneous spikes (Fig. 3.3d; n = 20; P = 0.18; paired t-test, two-sided). Our experiments directly demonstrate that the spike clusters seen following many propagation signal spikes result at least in part from activation of synapses originating from the single neuron identified by its propagation signal. These data indicate that stimulation at the electrode where a propagation signal was detected recapitulates the probability and amplitude characteristics of spontaneous events that resemble coupled spikes.

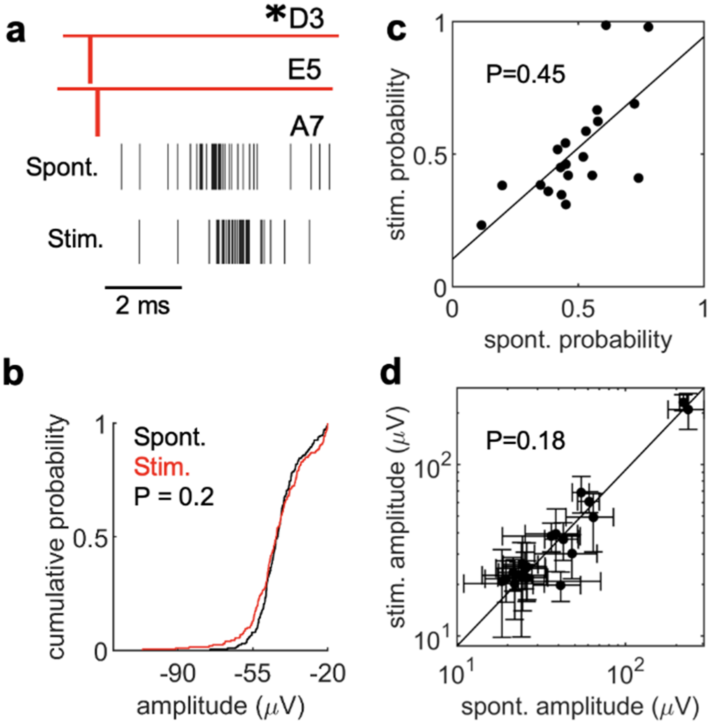

Figure 3.3: Stimulation of presynaptic neurons recapitulates spontaneous activity. a, 50 spontaneous co-occurring spikes in D3 and E5 were used as reference points to identify coupled spikes in A7 (spikes depicted as raster's below). Spiking activity in A7 after stimulation of electrode D3 using a 3μA biphasic current injection, 200 μsec total duration, 500 times. A blanking period (1.5 ms) during which no voltage data is collected is applied to all electrodes due to artifacts introduced by stimulation. For the stimulation experiments we therefore measured latency from the start of the stimulation period. b, The spike amplitude distribution of spikes detected at A7 (n = 200 randomly sampled spikes) after spontaneous propagation signals at D3/E5 (n = 572) is not significantly different than the spike distribution of spikes detected at A7 (n = 200 randomly sampled spikes, P = 0.2, two-sample KS test, two-sided, 1 MEA with 2 recording sessions for a and b)) after stimulation at electrode D3. c, Correlation of coupling probabilities for spontaneous activity versus stimulated activity. Each data point in (c) and (b) represents coupled neurons. Couplings were identified by identifying spontaneous propagation signal activity as references in a CCG and a coupling probability was assigned to the postsynaptic unit. Following identification of coupling relationships, electrodes associated with presynaptic propagation signals were then stimulated in order to obtain coupling probabilities with the same postsynaptic unit (n = 20 couplings, P = 0.45 paired t-test). d, For the same coupling events in (c), the correlation between spike amplitudes of the postsynaptic response in the spontaneous condition was compared to the spike amplitudes of the stimulated condition. Error bars represent the standard deviation of spike amplitude distributions (n = 20 couplings, P = 0.18 paired t-test, 3 MEAs and 6 total recording sessions were used for c and d).

3.1.4 Decreasing active synapse density lowers coupling probability

Presynaptic calcium influx initiates the release of neurotransmitters[45]. Cadmium (Cd^{2+}) reduces calcium conductance through calcium channels[46] and decreases the neurotransmitter release probability, and thus the number of active synapses[47]. However, the number of synapses between individual cultured hippocampal neurons can be sufficiently high such that single axons can make multiple synapses on the dendrites of single postsynaptic neurons[48, 49]. If coupled spikes result from integration of multiple synaptic inputs from single axons, then decreasing the number of active synapses with Cd^{2+} should decrease the coupling probability. We compared the coupling probabilities in control conditions and following the addition of Cd^{2+} (1μM, 5μM and 10 μM) in the same cultures. The majority of cases resembled the coupling between propagation signal F4/E5 and postsynaptic electrode H11, in which coupled spikes in control conditions were no longer present at 10 μM Cd^{2+} (Fig. 3.4a). We identified 83 functional couplings in control which decreased to 67 at 1 μM Cd^{2+}. Higher Cd^{2+} concentrations decreased the detection of coupling to 18 (5 μM Cd^{2+}) and 10 (10 μM Cd^{2+}). Interestingly, we saw no change in latency between control (2.9 ± 1.22, n = 83) and 5 μM Cd^{2+} (2.8 ± 0.77, n = 18). The total number of propagation signal spikes were comparable in all conditions (Fig. 3.4b), indicating that the cadmium-related decrease in coupling probability was unrelated to changes in number of propagation signal spikes, and thus neuronal activity. These results demonstrate that the coupling probability is sensitive to changes in the number of active neurotransmitter release sites.

To examine how decreasing the number of active synapses alters the connectivity of small neural networks, we used a recording that demonstrated a high level of coupling among propagation signals and asked how reduction of active synapses is affected with

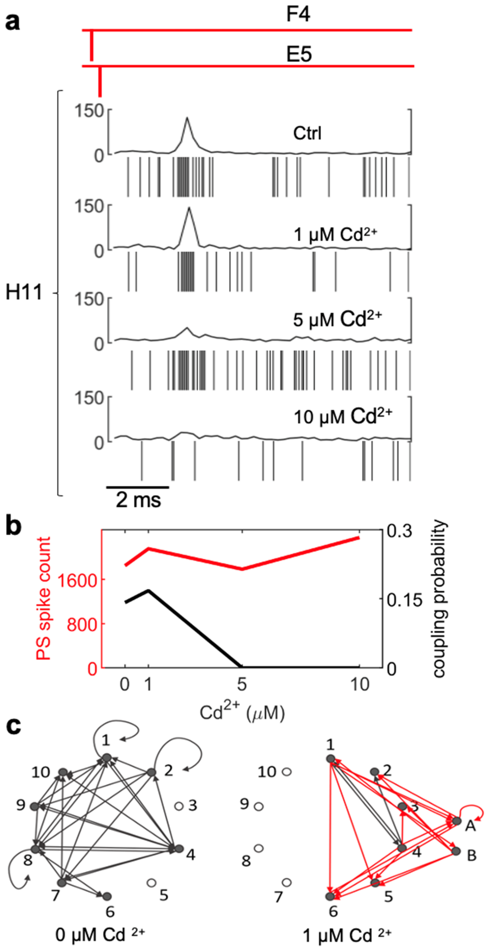

Figure 3.4: Cadmium alters coupling probabilities. a, Propagation signal eAP's detected at F4 and E5 with coupled spikes in H11 in the absence of cadmium and after addition of 1μM, 5μM, and 10μM cadmium. Coordinated spiking activity in H11 after propagation signal spikes in F4 and E5 decreased dramatically and resulted in the absence of coordinated activity at 10μM. b, In this example, the total number of spikes from the propagating neuron detected in electrode F4 to E5 under control conditions was 1848 spikes and the coupling probability of the postsynaptic unit at H11 was 0.14. Addition of 1μM Cd^{2+} resulted in 2154 spikes in the propagating neuron and a coupling probability of 0.16 with H11. At 5μM and 10μM Cd^{2+}, the spikes CCG at electrode H11 did not meet our criteria for coupling and were considered fully de-coupled; with 1784 and 2357 spikes in the propagating neuron, respectively. c, Network graphs were constructed to visualize the couplings between only propagation signal spiking activity. 8 of 10 propagation signals (nodes) formed a total of 29 couplings (black edges) in control conditions. Addition of 1μM Cd^{2+} resulted in loss of 26 edges present in control and the appearance of 17 couplings (red edges). No couplings were detected at 5μM or 10μM Cd^{2+} (1 MEA was used for 4 recording sessions for a – c).

1μM Cd^{2+}. Propagation signal neurons are represented by circles (nodes) in the network graph (Fig. 3.4c), and lines (edges) represent couplings between propagation signals. We identified 29 couplings (black edges) among 8 of 10 of the propagation signals in control conditions, including 3 recurrent connections. With the addition of Cd^{2+} only 3 of the 29 couplings present in control were retained (black lines, Fig. 3.4d, right). Interestingly, addition of Cd^{2+} revealed 17 couplings not seen in control conditions, including couplings among propagation signals that were only detected in Cd^{2+}. In this experiment, no couplings were detected in 5μM Cd^{2+}. The decrease in network connectivity in Cd^{2+} is consistent with reduction in the number of active synapses. Cd^{2+} also affects inhibitory neurons, and the consequent reduction in inhibitory tone may explain the redistribution of connections among existing and new propagation signals.

3.1.5 Temperature sensitivity of coupled eAP latency

Synaptic transmission is highly sensitive to temperature[37, 38, 50]. If postsynaptic activation and integration of multiple synapses from single axons is the basis for the eAP coupling latency, then changes in the coupling latency in response to temperature should be within range of previous measurements of synaptic delay[51, 52, 53]. Thus we measured the latency between propagation signal spikes and coupled spikes at three temperatures. As shown (Fig. 3.5a), increasing the temperature shifted the distribution of the coupled eAP latency to shorter values in this example (2.75 ± 0.47 ms at 30°C; 2.15 ± 0.1.09 ms at 32°C; 1.80 ± 0.91 ms at 36°C). The mean latency at 30°C (1.76 ± 0.8) was longer than at 36°C (1.41 ± 0.7; n = 23; $P < 0.0001$ paired t-test; Fig. 3.5b). The coupling latency captures the sum of events that occur between spiking in one neuron to spiking in another, including action potential propagation, the synaptic delay and synaptic integration. At physiological temperatures, the synaptic delay at mammalian synapses can range from

150 to 500 microseconds and can decrease by 50% within the temperature range of our experiments[52, 53]. Action potential propagation velocity increases by 30% between 30°C and 36°C 4. Plotting the change in coupling latency at 36°C as a function of the latency at 30°C (Fig. 3.5c) highlights the variability of the latency change in our data set. However, the mean coupling latency change between 30°C to 36°C (0.35 ± 0.32 ms, n = 23) is consistent with expected differences in temperature dependence of synaptic delay and action potential propagation. Interestingly, shorter coupling latencies at 30°C tended to have smaller temperature dependent changes, suggesting that these examples are close to the lower limit of our temporal resolution.

3.1.6 Contributions of multiple presynaptic neurons to spiking in a single postsynaptic neuron

The coupled eAPs we identified likely represent synaptic couplings. However, it is unlikely that activation of synapses from the majority of single axons reflects the most common source of action potentials in postsynaptic cells, given that most of our measurements of coupling probability were well below one. To address how multiple inputs influence a postsynaptic neuron, we used spike times from a single propagation signal to identify presynaptic couplings. In one example, we identified 7 inputs that were statistically coupled to the propagation signal eAPs. Of these, 5 inputs were propagation signals, and 2 were isolated as spikes from single electrodes (Fig. 3.6a). A raster display of eAPs from these 7 inputs highlights that the majority of presynaptic spikes occur 1 - 5 ms before the postsynaptic propagation signal eAPs (Fig. 3.6b). For each presynaptic input, the probability of a spike occurring 0.5 - 10 ms before the postsynaptic propagation signal eAP was computed as the ratio of the amount of post-synaptic spikes that has at least one presynaptic spike in the 9.5 ms window over the total number of post-synaptic

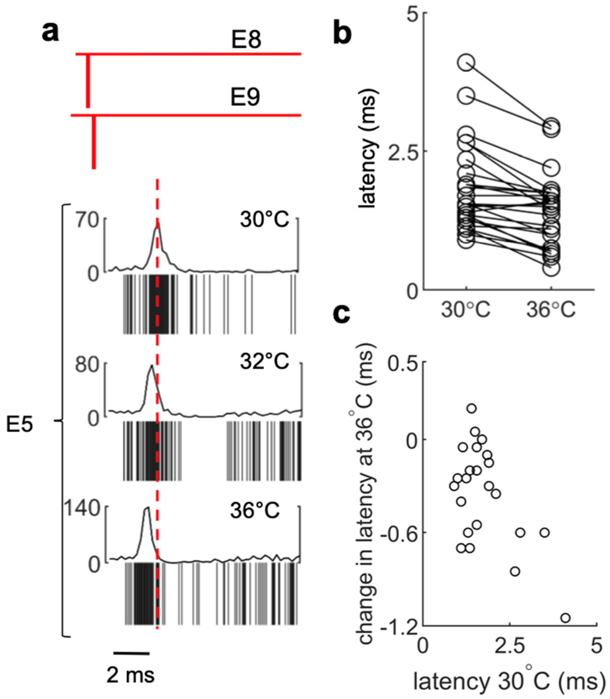

Figure 3.5: Temperature increase reduces coupling latency. a, Spikes from a propagating neuron detected at E8 and E9 coupled to a postsynaptic unit in E5. At 30°C the average latency between propagation signal spikes and the CCG peak in E5 was 2.75 ± 0.47 ms. Temperature in the same culture was increased to 32°C and 36°C sequentially, the average latency of the CCG peaks were 2.15 ± 1.09 ms and 1.80 ± 0.91 ms, respectively (1 MEA was used over 3 recording sessions for a). b, The distribution of average latency of presynaptic propagation signals coupled to postsynaptic units at 30°C is significantly different than the average latency of the same couplings at 36°C (1.76 ± 0.8 ms at 30°C, 1.41 ± 0.7 ms at 36°C; n = 23; $P < 0.0001$, paired t-test, two-sided). c, Average latency of couplings at 30°C versus the change in average latency of the same couplings at 36°C. (7 MEAs were used with 2 recording sessions per MEA, 14 total sessions, for b and c).

spikes. The coupling probabilities of the 7 inputs ranged from 0.09 to 0.31 (Fig. 3.6c). The low electrode density likely means that we do not capture all neurons presynaptic to the propagation signal neuron. Additionally, the relatively low coupling probabilities likely reflect the necessity for multiple well-timed co-active presynaptic inputs to bring a postsynaptic neuron to AP threshold.

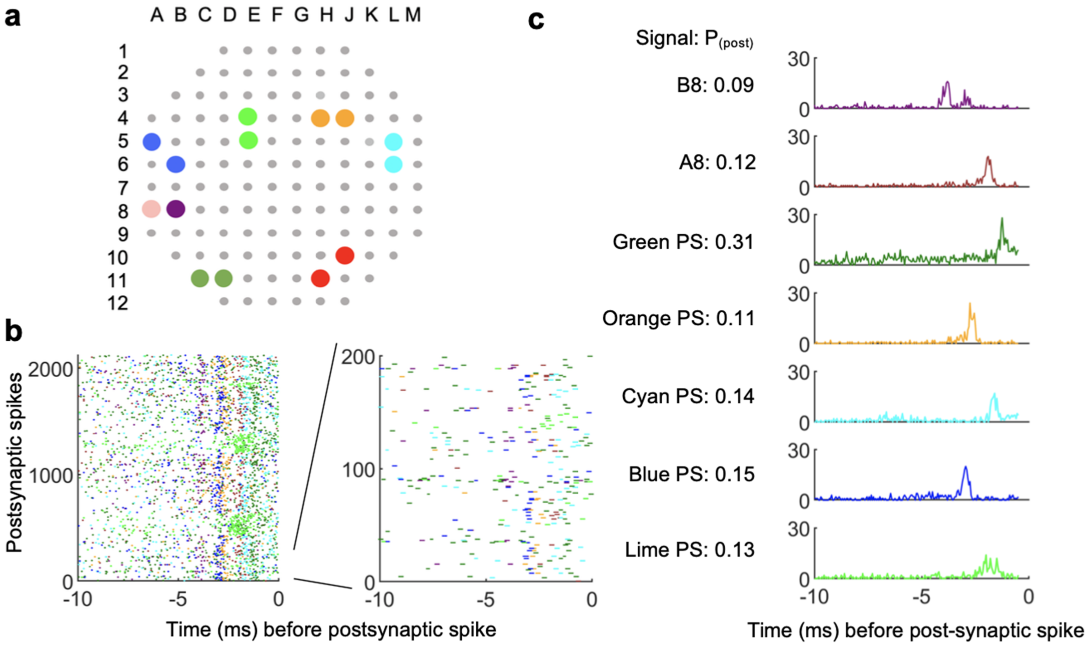

Figure 3.6: The influence of presynaptic inputs on a single postsynaptic propagation signal. a, Location of the post-synaptic neuron in red and upstream signals in other colors. Dots in different colors represent different upstream signals. Each two dots in the same color represent two anchor points for one propagation signal. Pink and purple represent two single electrode units. b, The patterns of pre-synaptic spikes. Each row shows the pre-synaptic firing pattern within 10ms prior to corresponding spike on the red neuron. The first 200 instances are zoomed in on the right. The colors are consistent with (a). c, CCGs for all upstream signals. Postsynaptic spikes (red propagation signal, n = 2124 spikes) were used as reference time points to perform CCG on other propagation signals and single electrodes A8 and B8. Because the postsynaptic spikes were used as the reference time points, the coupling probability was calculated by taking the ratio of presynaptic spikes in the CCG peak over the total number of postsynaptic spikes (1 MEA and a single recording session was used for a – c).

3.2 Methodology

3.2.1 Neuronal coupling detection algorithm

To facilitate identification of coupled spiking between two neurons we developed a set of algorithms for the automated detection of (1) propagation signals and (2) functionally coupled units (available at https://github.com/ZhuoweiCheng/Propagation-Signal-and-Synaptic-Coupling-Algorithm). For propagation signal detection, spike times were stored for all 120 electrodes in a cell array. The set of electrodes was denoted as E. To identify all propagation signals in an array, each electrode $e_i \in E$ was used as a reference electrode to compare with all electrodes e_j (j = 1, 2, . . . , n). Cross-correlograms (CCGs) were constructed using a 2 ms window before and after reference time-points for each (e_i, e_j) pair. Let n_{all} denote the number of spikes on the reference electrode and n_{win} denote the largest sum of counts in any 0.5 ms moving window in the cross-correlogram (CCG). A greater than 0.3 ratio indicates a consistent spike time delay of the target electrode with respect to the reference electrode. The ratio 0.3 was determined empirically with results from different thresholds compared with manually detected propagation signals. If a high ratio was detected in the CCG for (e_i, e_j), the delay time of e_j corresponding to e_i is recorded. All electrodes with high ratios were sorted based on their delay time. If all e_j have a non-negative delay time, then we can conclude that a propagation signal originating from ei was detected (Fig 3.2a). The process was repeated for all electrodes in the array generating a collection of propagation signals.

We then used the set of the identified propagation signals, denoted as S, to find instances of putative intercellular coupling. The putative functionally coupled relationships between all $s_i \in S$ or between $s_i \in S$ and $e_j \in E$ can be identified. To identify connections, we began with spike times from individual propagation signals. Spike times T_i for a propagation signal were computed using the spike times of the group of electrodes. Let

e_1 denote the earliest electrode on a signal and ex denote the electrode with the most spikes other than e_1. The spike times, T_i, are then computed with the average times of the co-occurrences in these two electrodes. Co-occurrences are defined as two spikes occurring in quick succession in separate electrodes.

We filtered our results as follows: (1) to minimize false-positive couplings, the lower limit of coupling probability was set to 0.1, (2) couplings with an average latency outside our window of interest (1 – 5 ms after the propagation signal eAP) were discarded as most central nervous system excitatory neurons couple to neighboring neurons with a latency within this range[54, 55], and (3) the area under the CCG peak must be 60% of the total area to avoid chance associations between pre- and postsynaptic spikes. To accomplish this, each signal s_i was used as a reference signal to compare with all other signals s_k (k $\neq$ i) or all electrodes e_j. A CCG, using a window between 0.5 and 10ms after reference time-points were performed for each (s_i, s_j) or (s_i, e_j) pair. The criteria for identifying connections are:

- If n_1 denotes the sum of counts of the CCG and n denotes the number of spikes in the reference signal, the ratio n_1/n must be larger than v_1.
- If n_2 denotes the largest sum of counts in any 3 ms moving window in the CCG, then the ratio n_2/n_1 must be larger than v_2.
- The delay time must be between v_3 and v_4 ms.
- The standard deviation for all the Δt in CCG is less than v_5.

The values used in this paper are v_1=0.1; v_2=0.57; v_3=1; v_4=5; v_5=2.7. Specifically, v_2 and v_5 were determined empirically. The value v_2 is a cutoff for the ratio of the number of spikes in the 3 ms moving window with the most spikes to the total number of spikes in the CCG. The larger the value of v_2, the stricter the criteria and the higher the certainty that the coupling results identified by the algorithm are real and non-random. However, the higher the value is for v_2, the more likely we are to exclude real couplings. The value v_5 is a threshold of the standard deviation of the latency. We used v_5 to filter out cases where one electrode detects eAPs from multiple nearby neurons, as can often happen in our recordings (data not shown). Between two electrodes, the coefficient of variation of eAP propagation latency should be small. It was often the case that single electrodes detected spikes from multiple neurons (for example Figures 3.1f and 3.2d) at the neuron densities we used. When spikes from multiple independent neurons are detected at any single electrode, the latency distribution of spikes between the target electrode and the reference electrode is expected to have large variability. All v_i can instead be user defined. If the relationship is between propagation signals and spikes at individual electrodes, the output of the algorithm also includes a verification flag. A flag value of one is a suggestion to manually verify the connection. Flag values are determined by comparing the normalized standard deviation of the voltage amplitude of all spikes on the target electrode to v_6. The value used in this paper for v_6 is 0.25.

3.2.2 Neuronal cell culture

The animal protocols and procedures in this study were approved by the Institutional Animal Care and Use Committee (IACUC) of University of California, Santa Barbara and were performed in accordance with the National Institutes of Health Guide for the Care and the Use of Laboratory Animals. All animal experiments were performed in accordance with ARRIVE guidelines.

We prepared hippocampal neurons from postnatal day 0 (P0) C57BL/6 male mice using a previously described protocol[56]. Up to 3 animals were used per experiment and the pooled hippocampal neurons were plated on multiple MEAs. Cleaned and sterilized multi-electrode arrays (120MEA100/30iR-ITO arrays; Multi Channel Systems) were coated with 0.1 mg/ml poly-L-lysine (Sigma-Aldrich) for 1h at $37°C$, rinsed 3 times with sterile water and air dried before plating. Plating was done in two steps. In the first step, cultured glial cells maintained in separate T-75 flasks were dissociated and plated (at 150,000 cells per well) on MEAs and allowed to proliferate. Once glia were confluent over the electrode area, freshly dissociated hippocampal cells were plated at 250,000 cells per dish (550 cells/mm^2) on the confluent glial cultures. Cultures were grown in minimum essential medium with Earle's salts (Thermo Scientific, catalog # 11090081) with 2mM Glutamax (Thermo Scientific), 5% heat-inactivated fetal bovine serum (Thermo Scientific), and 1 ml/l Mito+ serum extender (Corning) and supplemented with glucose to an added concentration of 21mM. For the purpose of long-term culturing and maintaining MEA sterility during recordings, the MEA chamber was covered with a membrane that permits CO_2 exchange when the plate is in the CO_2 incubator and during recordings.

3.2.3 MEA recordings

Extracellular voltage recordings of neuronal cultures were performed using an MEA 2100-System (Multichannel Systems, Reutlingen, Germany). Arrays contained 120 electrodes with a 100 μm inter-electrode distance. Voltage records were acquired at 20 kHz. All recordings were performed in culture media. The head stage temperature was set to $30°C$ with an external temperature controller and MEAs were equilibrated for 5 min on the head stage before data acquisition or after any pharmacological or temperature manipulation. Recording duration was typically 3 to 5 minutes. Only cultures at 14 days in vitro (DIV) or older were used for all pharmacological, stimulation and temperature experiments. These experiments used pooled neurons from up to 3 animals.

3.2.4 Data Processing

Raw extracellular voltage data from Multichannel Systems acquisition software was converted to HDF5 file format using Multichannel Data Manager software and processed offline. Using MEA tools[25], extracellular voltage records were bandpass filtered using a second order Butterworth filter with cutoff frequencies of 200Hz to 4000Hz followed by spike detection. Negative deflections in the voltage records were labelled as spikes when the amplitude exceeded 6 times the standard deviation of the median noise level. None of the data in this work was spike sorted. Spike times and amplitudes output from MEA Tools were used for subsequent analysis and development of automated algorithms in Matlab. Post-hoc analysis was performed in Matlab by extracting the raw voltages for electrodes of interest and inspecting the timing and amplitude of spikes within time windows of interest. In certain cases, to validate our results we shuffled spike times from electrodes of interest; spike time shuffling was done in a way that retained the inter-spike interval distribution from the spike train of interest to retain the overall spiking pattern. Propagation signals were differentiated from coupled signals based on the difference in inter-electrode latency. The inter-electrode latency of the propagation signals we detected had a mean of 0.46 ± 0.36 ms (n = 1014 electrode pairs). In contrast, the latencies of what we detected as coupled neurons had a mean of 2.79 ± 2.06 ms, (n = 746) in wild type neurons.

3.2.5 Statistical analysis

Statistical analysis was performed with Prism 8 or Matlab. Distributions were tested for normality using a one-sample Kolmogorov-Smirnov test. Non-uniformly distributed data were tested using non-parametric tests (two-sample Kolmogorov-Smirnov test or Mann-Whitney U-test) at a 5% significance level.

3.3 Discussion

In this work we present analytical approaches for detecting when synapses from single axons influence the ability of postsynaptic neurons to fire action potentials. Detection of action potential propagation validates that the preceding, presumably presynaptic, eAPs arise from single identifiable neurons. The timing of these eAPs is the clock we use to detect short latency spike clusters that follow, or even precede, propagating spikes.

Techniques such as simultaneous recordings with multiple patch clamp electrodes[57, 58], a combination of patch and extracellular recording[59, 60] and automated multi-patch recording[61] leave no doubt about the neuronal source of activity. However, the technically challenging nature of these methods makes their routine use difficult. The invasive nature of patch recording also precludes long-term monitoring of neurons. The results from our experiments would be difficult to obtain with other methodologies such as optical imaging methods that require fluorescence indicators resulting in phototoxicity and altered cell physiology[62]. By unambiguously isolating eAPs from single identifiable neurons, our methods demonstrate how synaptic coupling from multiple identified neurons can be simultaneously assessed, under a variety of experimental manipulations and/or across multiple days. High signal fidelity and temporal resolution with the MEA, capable of capturing spike amplitudes while recording from multiple sites, allowed us to infer a partial connectivity map for the culture (Fig. 3.4d). This "functional connectome" is clearly missing connectivity edges that are invisible due to the low electrode density relative to the density of the neurons and the presence of neurons outside the boundary of the array. However, another source of missing connectivity can be revealed when synaptic weights are changed as implemented by reducing the release probability (Fig. 3.4d). Reducing the number of active synapses with cadmium resulted in the expected loss of connections, but also the emergence of new connections, a latent connectivity network, probably due to suppression of inhibitory transmission. Likewise, detection of multiple inputs to a single neuron and determining each of their latencies and coupling probabilities (Fig. 3.6) presents novel approaches to dendritic signal summation[63, 64]. Our data revealed a multiplicity of input firing events within a 5 ms window that contribute, with different probabilities, toward eliciting a post synaptic action potential.

Chapter 4

Conclusion

Extracellular recording has been used for decades to non-invasively study excitable cells in a range of experimental contexts [3, 1, 6, 65]. Using extracellular recording to understand how neural networks integrate input, convert perception to electrical signal or respond to pharmacological or experimental manipulations requires unambiguous knowledge of the cellular source of each action potential in the data record. Discriminating the cellular source of any eAP becomes complicated because action potentials from multiple neurons can be detected by single electrodes (Figure 2.1F, 2.4B, 2.4E). This is especially true when neuron density is high. Post-acquisition data processing from contemporary MEAs requires automated approaches to identifying eAPs from single neurons.

Spike sorting routines are based on assumptions regarding how characteristics of eAP waveform heterogeneity correspond to the source neurons where those eAPs originate. Ground truth validation of spike sorting is not routinely available but has been achieved in technically challenging experiments pairing extracellular MEA recording with intra- or juxtacellular recording [15, 66]. As previously shown [31, 22] action potential propagation is reflected by two or more MEA electrodes with eAPs that repeatedly occur with short latency, in the same sequence (Figure 2.1B, C). Characteristics of propagating eAPs identify them as being from single neurons, in an analogous way that paired recording has been used to unambiguously isolate spikes from individual neurons.

In this dissertation we presented two algorithms that work with recordings from multi-electrode arrays. The first algorithm allows for automated detection of action potential propagation. When electrodes detect eAPs from multiple neurons, isolation of propagating eAPs by our algorithm labels spikes from each propagation as resulting from single neurons, even in a background of spikes from other cells. Multi-point detection inherent in our algorithm reinforces the reliability of our results. Isolation of eAP by using propagation makes no assumptions about waveform shapes. Our method of unambiguously isolating eAPs from multiple different neurons in each recording increase the utility of multi-electrode arrays for high content screening applications and could eventually be adapted for use in vivo, for example in retina [67].

Our second algorithm uses the information extracted from the first algorithm to non-invasively detect short latency relationships between neurons. Direct stimulation of presynaptic neurons validated our assertions. As expected, decreasing the number of active synapses with cadmium decreased the coupling probability. Given the timing and latency characteristics of what we define here as functional coupling, our data is most consistent with functional coupling representing the action of multiple synapses from a single axon acting on a single postsynaptic neuron in many cases. We cannot rule out that some of what we are detecting represents indirect synaptic coupling but for that to explain our data, the latencies and fidelity would have to be higher than expected from the literature. Our in vitro results are consistent with work in well characterized in vivo circuits[68, 69]. With this in vitro system we can screen the effects of pharmacological manipulations as well as the synaptic connectivity phenotypes from targeted mutant or iPS-derived neurons.

Bibliography

[1] B. Katz and R. Miledi, *The effect of calcium on acetylcholine release from motor nerve terminals*, *Proc R Soc Lond B Biol Sci* **161** (1965) 496–503.

[2] D. H. Hubel, *Tungsten microelectrode for recording from single units*, *Science* **125** (1957) 549–550.

[3] D. H. Hubel and T. N. Wiesel, *Receptive fields of cells in the striate cortex of very young, visually inexperienced kittens*, *J Neurophysiol* **26** (1963) 994–1002.

[4] H. Ju, M. R. Dranias, and V. A. M. J. Banumurthy, *Spatiotemporal memory is an intrinsic property of networks of dissociated cortical neurons*, *J Neurosci* **35** (2015) 4040–4051.

[5] J. J. J. al., *Fully integrated silicon probes for high-density recording of neural activity*, *Nature* **551** (2017) 232–236.

[6] B. J. Wainger, E. Kiskinis, C. Mellin, O. Wiskow, S. S. Han, J. Sandoe, N. P. Perez, L. A. Williams, S. Lee, G. Boulting, J. D. Berry, B. R. H. Jr, M. E. Cudkowicz, B. P. Bean, K. Eggan, and W. CJ., *Intrinsic membrane hyperexcitability of amyotrophic lateral sclerosis patient-derived neurons*, *Cell Rep* **7** (2014) 1–11.

[7] E. Slomowitz, B. Styr, I. Vertkin, H. Milshtein-Parush, I. Nelken, M. Slutsky, and I. Slutsky, *Interplay between population firing stability and single neuron dynamics in hippocampal networks*, *eLife* **4** (jan, 2015) e04378.

[8] N. X. Kodama, T. Feng, J. J. Ullett, H. J. Chiel, S. S. Sivakumar, and R. F. Galan, *Anti-correlated cortical networks arise from spontaneous neuronal dynamics at slow timescales*, *Sci Rep* **8** (2018), no. 666.

[9] A. Berényi, Z. Somogyvári, A. J. Nagy, L. Roux, J. D. Long, S. Fujisawa, E. Stark, A. Leonardo, T. D. Harris, and G. Buzsáki, *Large-scale, high-density (up to 512 channels) recording of local circuits in behaving animals*, *J Neurophysiol* **111** (2014) 1132–1149.

[10] G. T. Einevoll, F. Franke, E. Hagen, C. Pouzat, and K. D. Harris, *Towards reliable spike-train recordings from thousands of neurons with multielectrodes*, *Curr Opin Neurobiol* **22** (2012) 11–17.

[11] G. Hilgen, M. Sorbaro, S. Pirmoradian, J. O. Muthmann, I. E. Kepiro, S. Ullo, C. J. Ramirez, A. Puente Encinas, A. Maccione, L. Berdondini, V. Murino, D. Sona, F. Cella Zanacchi, E. Sernagor, and H. MH., *Unsupervised spike sorting for large-scale, high-density multielectrode arrays*, *Cell Rep* **18** (2017) 2521–2532.

[12] D. N. Hill, S. B. Mehta, and D. Kleinfeld, *Quality metrics to accompany spike sorting of extracellular signals*, *J Neurosci* **31** (2011) 8699–8705.

[13] R. Q. Quiroga, *Spike sorting*, *Curr Biol* **22** (2012) R45–R46.

[14] R. Diggelmann, M. Fiscella, A. Hierlemann, and F. Franke, *Automatic spike sorting for high-density microelectrode arrays*, *J Neurophysiol* **120** (2018) 3155–3171.

[15] P. Yger, G. L. Spampinato, E. Esposito, B. Lefebvre, S. Deny, C. Gardella, M. Stimberg, F. Jetter, G. Zeck, S. Picaud, J. Duebel, and O. Marre, *A spike sorting toolbox for up to thousands of electrodes validated with ground truth recordings in vitro and in vivo*, *eLife* **7** (mar, 2018) e34518.

[16] K. D. Harris, R. Q. Quiroga, J. Freeman, and S. L. Smith, *Improving data quality in neuronal population recordings*, *Nat Neurosci* **19** (2016) 1165–1174.

[17] G. Buzsáki, M. Penttonen, Z. Nádasdy, and A. Bragin, *Pattern and inhibition-dependent invasion of pyramidal cell dendrites by fast spikes in the hippocampus in vivo*, *PNAS* **93** (1996) 9921–9925.

[18] P. Stratton, A. Cheung, J. Wiles, E. Kiyatkin, P. Sah, and F. Windels, *Action potential waveform variability limits multi-unit separation in freely behaving rats*, *PLOS ONE* **7** (06, 2012) 1–16.

[19] M. C. Quirk and M. A. Wilson, *Interaction between spike waveform classification and temporal sequence detection*, *J Neurosci Methods* **94** (1999) 41–52.

[20] G. Hilgen, *Challenges for automated spike sorting: beware of pharmacological manipulations*, 2019.

[21] J. Magland, J. J. Jun, E. Lovero, A. J. Morley, C. L. Hurwitz, A. P. Buccino, S. Garcia, and A. H. Barnett, *Spikeforest, reproducible web-facing ground-truth validation of automated neural spike sorters*, *eLife* **9** (may, 2020) e55167.

[22] K. R. Tovar, D. C. Bridges, B. Wu, C. Randall, M. Audouard, J. Jang, P. K. Hansma, and K. KS., *Action potential propagation recorded from single axonal arbors using multielectrode arrays*, *J Neurophysiol* **120** (2018) 306–320.

[23] D. Debanne, E. Campanac, A. Bialowas, E. Carlier, and G. Alcaraz *Physiol Rev* **91** (2011) 555–602.

[24] E. Guzman, Z. Cheng, P. K. Hansma, L. R. Petzold, and K. S. Kosik, *Extracellular detection of neuronal coupling*, *Sci Rep* **19** (2021), no. 14733.

[25] D. C. Bridges, K. R. Tovar, B. Wu, P. K. Hansma, and K. S. Kosik, *Mea viewer: A high-performance interactive application for visualizing electrophysiological data*, *PLOS ONE* **13** (02, 2018) 1–10.

[26] H. V. Poor, *An Introduction to Signal Detection and Estimation.* Springer-Verlag, New York, 1994.

[27] Y. Grossman, I. Parnas, and S. ME., *Mechanisms involved in differential conduction of potentials at high frequency in a branching axon*, *J Physiol* **295** (1979) 307–322.

[28] A. F. Soleng, A. Baginskas, P. Andersen, and M. Raastad, *Activity-dependent excitability changes in hippocampal ca3 cell schaffer axons*, *J Physiol* **560** (2004) 491–503.

[29] C. L. Cox, W. Denk, D. W. Tank, and K. Svoboda, *Action potentials reliably invade axonal arbors of rat neocortical neurons*, *Proc Natl Acad Sci USA* **97** (2000) 9724–9728.

[30] M. Raastad and G. M. Shepherd, *Single-axon action potentials in the rat hippocampal cortex*, *J Physiol* **548** (2003) 745–752.

[31] D. J. Bakkum, U. Frey, M. Radivojevic, T. L. Russell, J. M"uller, M. Fiscella, H. Takahashi, and A. Hierlemann, *Tracking axonal action potential propagation on a high-density microelectrode array across hundreds of sites*, *Nat Commum* **4** (2013), no. 2181.

[32] M. B. Jackson, A. Konnerth, and G. J. Augustine, *Action potential broadening and frequency-dependent facilitation of calcium signals in pituitary nerve terminals*, *PNAS* **88** (1991) 380–384.

[33] P. W. Liu, N. T. Blair, and B. P. Bean, *Action potential broadening in capsaicin-sensitive drg neurons from frequency-dependent reduction of kv3 current*, *J Neurosci* **37** (2017) 9705–9714.

[34] M. S. Fee, P. P. Mitra, and D. Kleinfeld, *Variability of extracellular spike waveforms of cortical neurons*, *J Neurophysiol* **76** (1996) 3823–3833.

[35] C. M. Colbert, J. C. Magee, D. A. Hoffman, and D. Johnston, *Slow recovery from inactivation of na+ channels underlies the activity-dependent attenuation of dendritic action potentials in hippocampal ca1 pyramidal neurons*, *J Neurosci.* **17** (1997) 6512–21.

[36] G. Buzsáki, C. A. Anastassiou, and C. Koch, *The origin of extracellular fields and currents - eeg, ecog, lfp and spikes*, *Nat Rev Neurosci* **13** (2012) 407–420.

[37] R. A. Chapman, *Dependence on temperature of the conduction velocity of the action potential of the squid giant axon*, *Nature* **213** (1967) 1143–1144.

[38] D. N. Franz and A. Iggo, *Conduction failure in myelinated and non-myelinated axons at low temperatures*, *J Physiol* **199** (1968) 319–345.

[39] T. Sharf, T. van der Molen, E. Guzman, S. M. Glasauer, G. Luna, Z. Cheng, M. Audouard, K. G. Ranasinghe, K. Kudo, S. S. Nagarajan, K. R. Tovar, L. R. Petzold, P. K. Hansma, and K. S. Kosik, *Intrinsic network activity in human brain organoids*, *bioRxiv* (2021) [https://www.biorxiv.org/content/early/2021/01/28/2021.01.28.428643.full.pdf].

[40] M. A. Lancaster, M. Renner, M. C-a, D. Wenzel, L. S. Bicknell, M. E. Hurles, T. Homfray, J. M. Penninger, A. P. Jackson, and J. A. Knoblich, *Cerebral organoids model brain development and microcephaly*, *Nature* **501** (2013) 373–379.

[41] K. Mhp, S. U. Ilschner, B. M. Kampa, S. R. Williams, P. C. Ruben, and G. J. Stuart, *Action potential generation requires a high sodium channel density in the axon initial segment*, *Nat Neurosci* **11** (2008) 2008.

[42] M. Radivojevic, F. Franke, M. Altermatt, J. Müller, A. Hierlemann, and D. J. Bakkum, *Tracking individual action potentials throughout mammalian axonal arbors*, *eLife* **6** (oct, 2017) e30198.

[43] B. L. McNaughton, J. O'Keefe, and C. A. T. s. A. Barnes, *new technique for simultaneous isolation of several single units in the central nervous system from multiple unit records*, *Journal of Neuroscience Methods* **8** (1983) 391–397.

[44] C. Rossant, S. Kadir, D. Goodman, *et. al.*, *Spike sorting for large, dense electrode arrays*, *Nature Neuroscience* **19** (2016) 634–641.

[45] J. del Castillo and L. Stark, "The effect of calcium ions on the motor end-plate potentials." 1952.

[46] J. B. Lansman, P. Hess, and R. W. Tsien, *Blockade of current through single calcium channels by cd2+, mg2+, and ca2+. voltage and concentration dependence of calcium entry into the pore*, *J. Gen. Physiol* **88** (1986) 321–347.

[47] J. S. Diamond and C. E. Jahr, *Asynchronous release of synaptic vesicles determines the time course of the ampa receptor-mediated epsc*, *Neuron* **15** (1995) 1097–1107.

[48] S. Mennerick, J. Que, A. Benz, and C. F. Zorumski, *Passive and synaptic properties of hippocampal neurons grown in microcultures and in mass cultures*, *Journal of Neurophysiology* **73** (1995) 320–332.

[49] M. Ivenshitz and M. Segal, *Neuronal density determines network connectivity and spontaneous activity in cultured hippocampus*, *Journal of Neurophysiology* **104** (2010) 1052–1060.

[50] B. L. Sabatini and W. G. Regehr, *Timing of synaptic transmission*, *Annu. Rev. Physiol.* **61** (1999) 521–542.

[51] J. G. Borst, F. Helmchen, and B. Sakmann, *Pre- and postsynaptic whole-cell recordings in the medial nucleus of the trapezoid body of the rat*, *J Physiol* **489** (1995) 825–840.

[52] B. L. Sabatini and W. G. Regehr, *Timing of neurotransmission at fast synapses in the mammalian brain*, *Nature* **384** (1996) 170–172.

[53] H. Taschenberger and H. v. Gersdorff, *Fine-tuning an auditory synapse for speed and fidelity: Developmental changes in presynaptic waveform, epsc kinetics, and synaptic plasticity*, *J. Neurosci.* **20** (2000) 9162–9173.

[54] H. Markram, J. L"ubke, M. Frotscher, A. Roth, and B. Sakmann, *Physiology and anatomy of synaptic connections between thick tufted pyramidal neurones in the developing rat neocortex*, *J Physiol* **500** (1997) 409–440.

[55] R. M. Fitzsimonds, H. Song, and M. Poo, *Propagation of activity-dependent synaptic depression in simple neural networks*, *Nature* **388** (1997) 439–448.

[56] K. R. Tovar and G. L. Westbrook, *Amino-terminal ligands prolong nmda receptor-mediated epscs*, *J. Neurosci.* **32** (2012) 8065–8073.

[57] G. Silberberg, C. Wu, and H. Markram, *Synaptic dynamics control the timing of neuronal excitation in the activated neocortical microcircuit*, *J Physiol* **556** (2004) 19–27.

[58] Y. Wang *et. al.*, *Heterogeneity in the pyramidal network of the medial prefrontal cortex*, *Nature Neuroscience* **9** (2006) 534–542.

[59] R. Vardi, A. Goldental, S. Sardi, A. Sheinin, and I. Kanter, *Simultaneous multi-patch-clamp and extracellular-array recordings: Single neuron reflects network activity*, *Sci Rep* **6** (2016) 1–9.

[60] D. J"ackel *et. al.*, *Combination of high-density microelectrode array and patch clamp recordings to enable studies of multisynaptic integration*, *Sci Rep* **7** (2017) 1–17.

[61] Y. Peng, F. X. Mittermaier, H. Planert, U. C. Schneider, H. Alle, and J. R. P. Geiger, *High-throughput microcircuit analysis of individual human brains through next-generation multineuron patch-clamp*, *eLife* **8** (nov, 2019) e48178.

[62] J. H. Stockley, M. Evans, K.and Matthey, *et. al.*, *Surpassing light-induced cell damage in vitro with novel cell culture media*, *Scientific Reports* **7** (2017), no. 849.

[63] T. Branco and M. H"ausser, *Synaptic integration gradients in single cortical pyramidal cell dendrites*, *Neuron* **69** (2011) 885–892.

[64] N. Xu *et. al.*, *Nonlinear dendritic integration of sensory and motor input during an active sensing task*, *Nature* **492** (2012) 247–251.

[65] A. Fernández-Ruiz, A. Oliva, E. Fermino de Oliveira, F. Rocha-Almeida, and G. Tingley, A. Buzsáki, *Long-duration hippocampal sharp wave ripples improve memory*, *Science* **364** (2019) 1082–1086.

[66] C. A. Anastassiou, R. Perin, G. Buzsáki, H. Markram, and C. Koch, *Cell type and activity-dependent extracellular correlates of intracellular spiking*, *J Neurophysiol* **114** (2015) 608–623.

[67] P. H. Li, J. L. Gauthier, M. Schiff, A. Sher, D. Ahn, G. D. Field, M. Greschner, E. M. Callaway, A. M. Litke, and E. J. Chichilnisky, *Anatomical identification of extracellularly recorded cells in large-scale multielectrode recordings*, *J Neurosci* **35** (2015) 4663–4675.

[68] L. Marshall, D. Henze, H. Hirase, X. Leinekugel, G. Dragoi, and B. G., *Hippocampal pyramidal cell-interneuron spike transmission is frequency dependent and responsible for place modulation of interneuron discharge*, *J. Neurosci.* **22** (2002).

[69] D. F. English, S. McKenzie, T. Evans, K. Kim, E. Yoon, and G. Buzsáki, *Pyramidal cell-interneuron circuit architecture and dynamics in hippocampal networks*, *Neuron* **96** (2017), no. 2 505–520.e7.